U. S. NAVAL ORDNANCE TEST STATION

W. W. Hollister, Capt., USN
Commander

Wm. B. McLean, Ph.D.
Technical Director

NOTS TP 2569 NAVWEPS REPORT 7584

WATER-TUNNEL TESTS OF A BASE-VENTED HYDROFOIL HAVING A CAMBERED PARABOLIC CROSS SECTION

By

Thomas G. Lang
and
Dorothy A. Daybell

Research Department

Copy 255

China Lake, California
10 October 1960

NOTS Technical Publication 2569
NAVWEPS Report 7584

Published by ..... Research Department
Manuscript 508/MS-6
Collation ..... Cover, 38 leaves, abstract cards
First printing ..... 280 numbered copies
Security classification ..... UNCLASSIFIED

FOREWORD

The Research and Underwater Ordnance Departments of the U. S. Naval Ordnance Test Station have been engaged in an experimental and theoretical investigation of vented hydrofoils. This report gives results of water-tunnel tests on a base-vented hydrofoil having a cambered parabolic cross section, conducted in November and December 1958.

The test work was conducted under an extension of California Institute of Technology Task Assignment NOrd 16200. Data analysis and presentation were conducted under Bureau of Ordnance Task Assignment NO-404-664/41001/01060.

This report was reviewed for technical accuracy by Henry Yerby and Howard Kelly of this Station.

WM. B. MC LEAN
Technical Director
and Acting Head,
Research Department

ABSTRACT

Results of water-tunnel tests on a base-vented hydrofoil having a cambered parabolic cross section show lift-to-drag ratios of 24 for an infinite aspect ratio and 8.5 for an aspect ratio of 1.44 at the minimum ventilation numbers attained.

The drag coefficients measured are in good agreement with linearized cavity theory. The measured lift and moment coefficients are in agreement with wind-tunnel tests of airfoils with streamlined cross sections having the same camber line.

The air cavity produced behind the base does not spring forward to the leading edge unless the hydrofoil has stalled or excessive cavitation occurs behind the leading edge.

CONTENTS

NOMENCLATURE

a	Fraction of chord, from leading edge of hydrofoil, over which design load is uniform
A	Planform area of hydrofoil (bc), ft^2
A_b	Base area of hydrofoil (bt), ft^2
A_x	Area of chordwise cross section of hydrofoil model, ft^2
A_o	Effective cross-sectional area of rectangular working section of water tunnel (exclusive of boundary layer) at static-pressure tap, ft^2
A_1	Effective cross-sectional area of rectangular working section of water tunnel (exclusive of boundary layer) at spindle axis, ft^2
A_2	Effective cross-sectional area of circular-segment working section of water tunnel (exclusive of boundary layer) at static-pressure tap, ft^2
$\mathfrak{R}$	Aspect ratio of hydrofoil when cantilevered from one wall (2b/c)
b	Span of hydrofoil, ft
B_o	Horizontal static-pressure gradient in rectangular working section of water tunnel, ft^{-1}
B_2	Horizontal static-pressure gradient in circular-segment working section of water tunnel, ft^{-1}
c	Chord of hydrofoil, ft
C_D	Drag coefficient ($D/q_\infty A$)
C_D^*	Average value of (C_D - minimum C_D) over various K values with finite $\mathfrak{R}$
C_{D_c}	Pressure drag coefficient produced by cavity or separated wake

C_{D_f}	Frictional drag coefficient
C_{D_i}	Induced drag coefficient
C_{D_s}	Separation drag coefficient
$C_{D_{s(o)}}$	Separation drag coefficient at $C_L = 0$
C_{D_t}	Hydrofoil-tip drag coefficient
C_L	Lift coefficient $(L/q_\infty A)$
C_{L_d}	Design lift coefficient
C_{L_o}	Lift coefficient at $\alpha = 0°$, infinite aspect ratio
C'_{L_o}	Lift coefficient at $\alpha = 0°$, finite aspect ratio
C_{L_α}	Lift coefficient derivative, infinite aspect ratio, per radian
C'_{L_α}	Lift coefficient derivative, finite aspect ratio, per radian
C_M	Pitching-moment coefficient (about quarter-chord point) $(M/q_\infty Ac)$
C_{M_o}	Pitching-moment coefficient at $\alpha = 0°$
C_{M_α}	Pitching-moment coefficient derivative, per radian
C_p	Local pressure coefficient $(P - P_\infty)/q_\infty$
D	Drag, lb
D'	Drag coefficient $(D/q_\infty A_b)$
h	Height of water-tunnel working section, ft
h_e	Height of equivalent rectangular water-tunnel working section, ft
K	Ventilation number $(P_\infty - P_c)/q_\infty$
L	Lift, lb
L/D	Lift-to-drag ratio
M	Pitching moment about quarter-chord point, ft-lb

p_1 Perimeter of rectangular tunnel cross section at spindle axis, ft

p_3 Perimeter of circular-segment tunnel cross section at spindle axis, ft

P Local static pressure on surface of hydrofoil, lb/ft^2

P_c Base or cavity pressure, lb/ft^2

P_ℓ Pressure in high-pressure air-supply line, lb/ft^2

P_{min} Minimum pressure on surface of hydrofoil, lb/ft^2

P_s Standard pressure for air-flow meter calibration, 2,120 lb/ft^2

P_v Vapor pressure of water, lb/ft^2

P_∞ Free-stream static pressure, lb/ft^2

P_o Static pressure at static-pressure tap in rectangular working section, lb/ft^2

P_1 Static pressure at spindle axis in rectangular working section of tunnel, lb/ft^2

q_∞ Free-stream dynamic pressure $\left(\frac{1}{2}\rho V_\infty^2\right)$, lb/ft^2

q_o Dynamic pressure at static-pressure tap in rectangular working section of tunnel, lb/ft^2

q_1 Dynamic pressure at spindle axis in rectangular working section of tunnel, lb/ft^2

Q Air-flow rate at free-stream static pressure $Q_m \frac{P_\ell}{P_\infty}\sqrt{\frac{P_s}{P_\ell}}$ as derived in Appendix C , ft^3/sec

Q' Air-flow-rate coefficient $(Q/V_\infty A_b)$

Q_ℓ Air-flow rate in high-pressure supply line, ft^3/sec

Q_m Air-flow meter reading, ft^3/sec

r' Ratio of leading-edge radius to chord length

R_c Reynolds number $(V_\infty c/\nu)$

t Base thickness of hydrofoil, ft

t_c Maximum thickness of cavity, ft

V Flow velocity on hydrofoil surface, ft/sec

V_c Increment of flow velocity on hydrofoil due to camber, ft/sec

V_{max} Maximum flow velocity at some point on hydrofoil surface, ft/sec

V_t Flow velocity on uncambered hydrofoil at zero angle of attack for a given thickness distribution, ft/sec

V_∞ Free-stream velocity, ft/sec

V_o Tunnel velocity at static-pressure tap in rectangular working section, ft/sec

V_1 Tunnel velocity at axis of spindle in rectangular working section, ft/sec

V_a Increment of flow velocity on hydrofoil due to angle of attack

x Distance from leading edge along chord of hydrofoil, ft; (in Appendix B, distance along tunnel center line, ft)

x' x/c

x_t Distance along tunnel center line from static-pressure tap to spindle axis

y Distance perpendicular to chord of hydrofoil, ft

α Angle of attack, radians, unless otherwise stated

α_d Design angle of attack, radians, unless otherwise stated

α_m Angle of attack at which drag coefficient is a minimum, radians

ΔC_L $C_{L_{free\ stream}} - C_{L_{measured}}$ (similarly for other coefficients)

θ Displacement thickness of boundary layer, ft

ν Kinematic viscosity of water, ft^2/sec

ρ Mass density of water, $slug/ft^3$

σ Free-stream cavitation number $(P_\infty - P_v)/q_\infty$

σ_i Incipient cavitation number, value of σ at which hydrofoil begins to cavitate

τ t/c

INTRODUCTION

The purpose of this experimental study was to investigate a new type of hydrofoil cross section that might be useful for propellers, pumps, and the lifting surfaces of hydrofoil-supported craft.

Until recently, the commonly used hydrofoils had streamlined cross sections, and operated fully wetted. The efficiency of streamlined hydrofoils is high until they begin to cavitate. As cavitation increases, their surfaces become pitted, noise is generated, and, most important, drag increases, and lift becomes unsteady and eventually begins to decrease.

Supercavitating hydrofoils have recently been developed by the Navy at the David Taylor Model Basin (Ref. 1). The cross section of these hydrofoils consists of a thin, sharp leading edge, a thick, blunt trailing edge, and usually a concave lower surface. In operation, a cavity springs rearward from the leading edge on the upper side and collapses behind the trailing edge. The efficiency of supercavitating hydrofoils is lower than that of fully wetted hydrofoils, but the lift force is steady at all speeds. By introducing gas into the cavity it can be maintained at low speeds and the cavitation noise reduced. This modification is sometimes called a superventilating hydrofoil.

The hydrofoil tested in this experimental program had a parabolic cross-sectional thickness distribution with a blunt base, and was cambered using the NACA a = 1.0 camber line. The parabolic thickness distribution was selected because the speed at which vapor cavitation begins is not a function of thickness, as in the streamlined cross sections, but of the angle of attack and the camber. The drag of this hydrofoil can be considerably reduced by introducing gas behind the base, making it a "base-vented" hydrofoil. The resulting drag is slightly greater than that of a streamlined hydrofoil and increases with increasing base thickness. The advantage of this cross section is that it is less susceptible to vapor cavitation than streamlined cross sections and has greater strength than other high-speed hydrofoils, with an efficiency lying between those of the streamlined hydrofoils and the superventilating hydrofoils. A discussion of base-

vented hydrofoils, including a description of a typical family and estimates of their efficiency and cavitation resistance, is presented in Ref. 2.

The experiments reported here were performed in the autumn of 1958 in the High-Speed Water Tunnel at the California Institute of Technology (CIT). They followed a series of similar experiments on streamlined hydrofoils that were vented by forcing air through ports in their surfaces (Ref. 3). The measurements include lift, drag, moment, base-cavity pressure, air-flow rate, and incipient cavitation number. The independent variables were tunnel velocity and static pressure, angle of attack, and air-flow rate. The aspect ratios AR for the model were ∞ and 1.44.

EXPERIMENTAL APPARATUS AND PROCEDURE

The CIT High-Speed Water Tunnel is described in detail in Ref. 4. Parallel vertical plates were installed in the original circular working section to form a two-dimensional channel (Ref. 5). For the finite aspect ratio tests one side plate was removed. The hydrofoil model was attached to a rigid, hollow spindle connected to the water-tunnel force balance. The hydrofoil end-gap at the spindle was eliminated by attaching the hydrofoil to the spindle through a 5.00-inch-diameter disk set flush with the channel wall (as seen in Fig. 12). The hydrofoil-disk-spindle assembly was rotated manually to vary the angle of attack. Tubing for measuring the cavity pressure and for ducting air was introduced to the model through the hollow spindle. The rate of air flow to the model was varied manually by means of a pressure regulator in the high-pressure air line at CIT. Figure 1 shows the hydrofoil model and the air-flow and pressure instrumentation.

DESCRIPTION OF THE MODEL

The hydrofoil model used for this experiment had a parabolic thickness distribution, cambered to a design lift coefficient of 0.4, with the NACA a = 1.0 (uniform-load) camber line described in Ref. 6. It had a 4-inch chord, a 2.95-inch span, and a thickness-to-chord ratio of 0.15. The hydrofoil is shown in Fig. 2 and 3 and its ordinates are given in Appendix A. There were two holes in the base, one near the spindle end for ventilating the base, the other at midspan for measuring the cavity pressure.

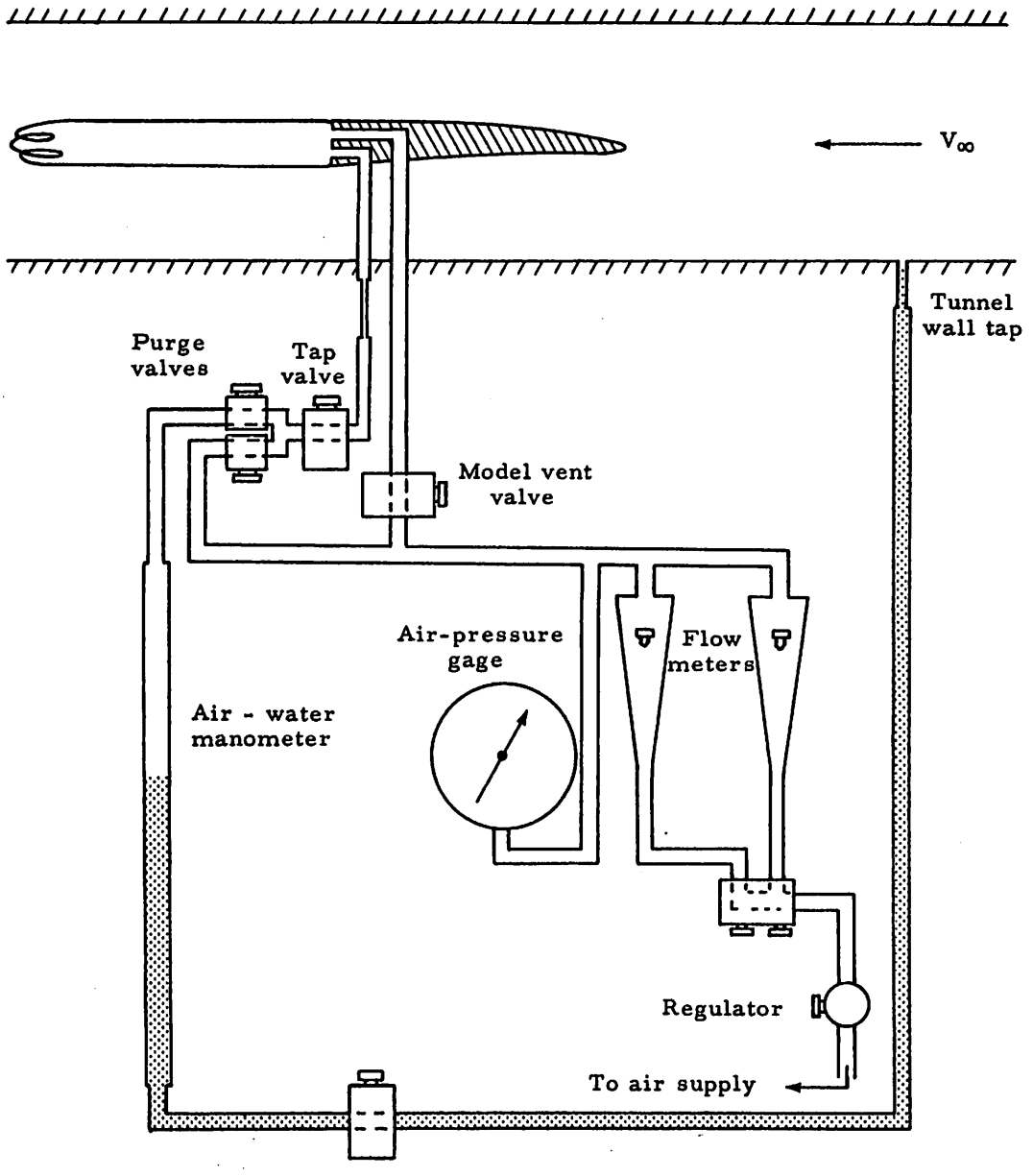

FIG. 1. Vented Hydrofoil System.

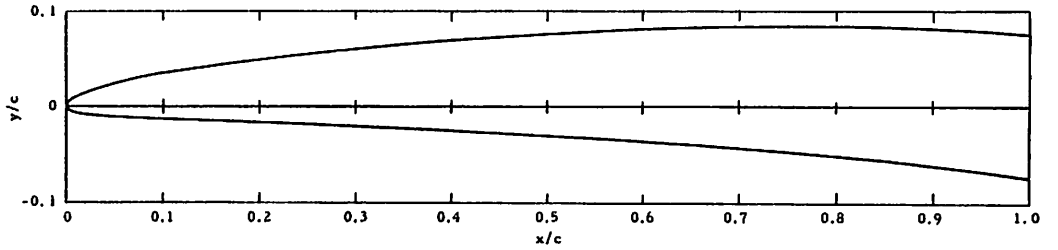

FIG. 2. Cross Section of Hydrofoil Model.

INSTRUMENTATION

Lift, drag, and moment were measured on the force balance described in Ref. 4 and 7. The forces were indicated on dial pressure gages and readout counters, calibrated to indicate directly pounds of lift and drag and inch-pounds of moment. The readings from the dial pressure gages were found to be sufficiently accurate for this experiment (±0.5% or better).

Air-cavity pressures were measured by an air-water manometer. The line from the model tap was purged of water with a blast of air before a reading was made. The same manometer was used to measure the base pressure in fully wetted flow; the bottom of the manometer was connected to the model tap and the top was left open to the atmosphere. These measurements were accurate within 0.01 foot of water.

The static pressure in the working section was measured with a mercury barometer; the pressure tap was located in the working-section wall, 5 inches upstream from the midchord point of the model. The dynamic-pressure measurement was obtained by measuring the static-pressure difference across the nozzle, using a differential water-mercury manometer. These measurements should be accurate within 0.01 foot of mercury.

The air-flow rate was measured with a float-type flowmeter, and the air pressure with a precision dial gage. The accuracy of the air-flow-rate measurement should be within 5%.

To supplement these measurements, simultaneous top-view and side-view still photographs were taken at most of the data points, using electrically operated 35-mm microfilm cameras with an exposure time of approximately 10 microseconds.

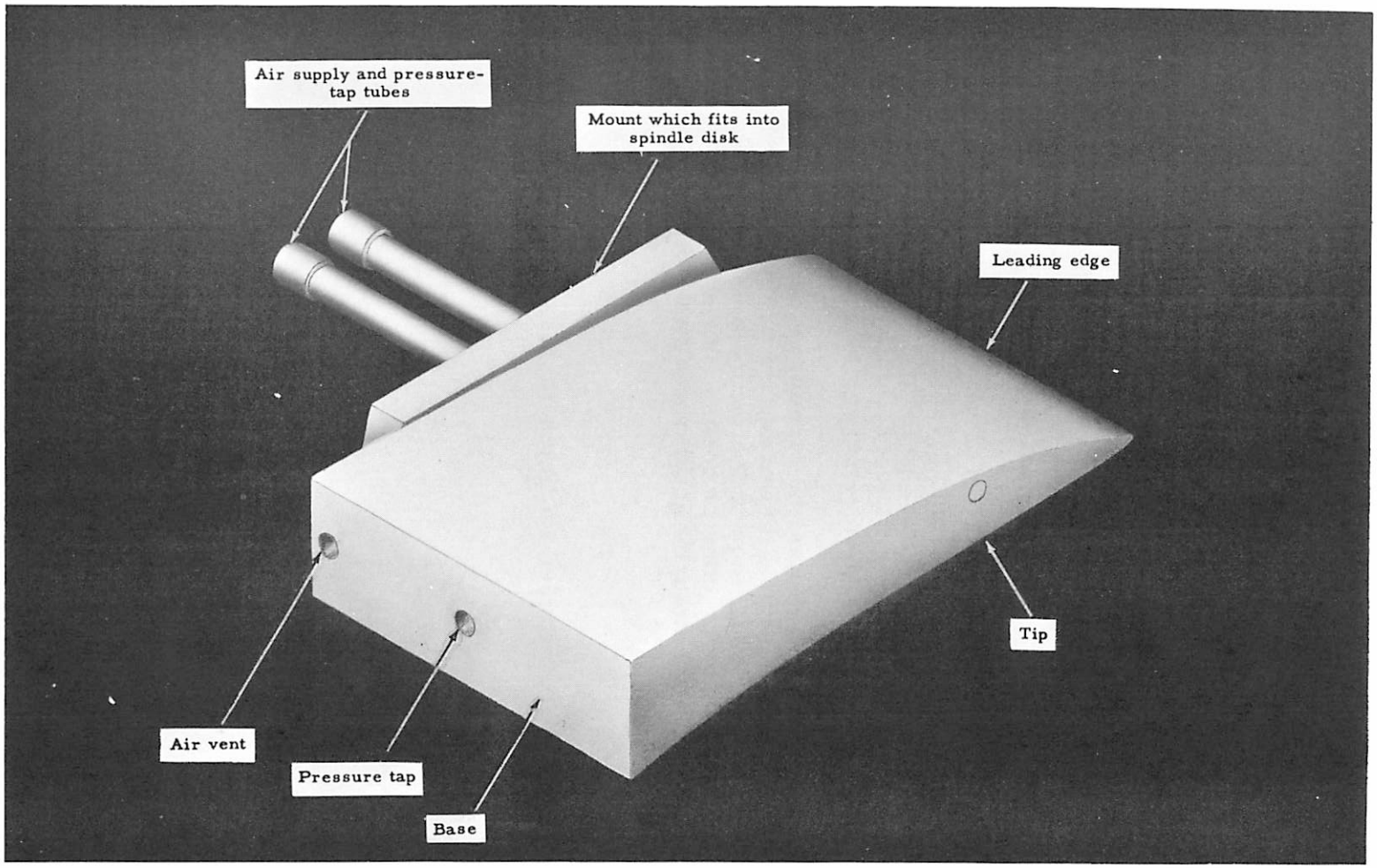

FIG. 3. Hydrofoil Model.

TEST PROCEDURE

During each run, the velocity, static pressure, and angle of attack were held constant while the air-flow rate was varied in steps. First the forces were recorded without air flow; then the air-flow rate was gradually increased until no further decrease was noted in the drag reading. After the forces and the cavity pressure had been recorded, the air-flow rate was decreased by steps and the forces and the cavity pressure were recorded at each step. These data were recorded manually from the gages and manometers. Whenever there were large oscillations in a force or pressure, the average value as well as the upper and lower limits were recorded.

The runs were made at tunnel velocities of 20, 30, and 40 ft/sec, with the tunnel static pressure varying from 2,090 to 3,820 lb/ft^2. Most of the data were obtained at pressures of 2,287 and 2,090 lb/ft^2 and at velocities of 30 and 20 ft/sec.

During most of the tests the stream velocity was automatically maintained. In some runs, however, the air exhausted into the tunnel reduced the efficiency in the diffuser section of the tunnel, making manual velocity control necessary. In these cases the dynamic-pressure measurement was used to compute the velocity.

DATA REDUCTION

The data were reduced to dimensionless coefficients as follows:

Lift coefficient $$C_L = \frac{\text{Lift}}{q_\infty A}$$

Drag coefficients $$C_D = \frac{\text{Drag}}{q_\infty A}$$

$$D' = \frac{\text{Drag}}{q_\infty A_b}$$

Pitching moment coefficient (about quarter-chord point) $$C_M = \frac{\text{Pitching moment}}{q_\infty A c}$$

Ventilation number	$K = \frac{P_\infty - P_c}{q_\infty}$
Air-flow-rate coefficient	$Q' = \frac{Q}{V_\infty A_b}$
Free-stream cavitation number	$\sigma = \frac{P_\infty - P_v}{q_\infty}$
Lift-to-drag ratio	L/D

In calculating the force, ventilation, and cavitation coefficients, corrections were applied for spindle-disk tare forces and tunnel-wall interference effects.

The spindle-disk tare corrections were obtained from Ref. 5, where the drag tare was found to be the only significant correction. The tares were measured by mounting the hydrofoil on the wall opposite the spindle and repeating typical force runs. Although the hydrofoil used in Ref. 5 had a different cross section, the drag-tare correction is considered valid for the parabolic hydrofoil, since the small difference in cross section would not materially change the wetted area of the 5-inch-diameter spindle disk used for both tests. The drag-coefficient correction, based on the planform area A, varied with α between 0.0035 and 0.0053. However, Ref. 5 did not furnish the effects on disk drag of the air cavity, end-gap clearance, and wall-hydrofoil boundary-layer interference. Because of this, and because there is no valid reason for a variation of disk drag with α, a constant spindle-disk drag correction of $\Delta C_D = 0.0045$, or $\Delta D' = 0.030$, was used.

The force and pressure data were corrected for solid and wake blockage, lift effect, and working-section horizontal-pressure gradient, using the standard wind-tunnel techniques of Ref. 8. The corrections calculated for a fully wetted hydrofoil were applied to both the fully wetted and base-vented cases. Tunnel corrections were applied to the data points of all the figures in this report, except Fig. 25 and 26, in which the magnitudes of the various corrections are shown.

A full description of tunnel-interference corrections is given in Appendix B. The method of reducing the air-flow-rate data is given in Appendix C.

RESULTS AND ANALYSIS

DESCRIPTION OF FLOW

When the hydrofoil model was fully wetted and the static pressure in the tunnel reduced, the vortices behind the blunt base were visible wherever their centers cavitated (Fig. 4). Additional cavitation was seen near the leading edge when the angle of attack was increased. These phenomena are normal and can be expected to occur as the static pressure drops.

When the static pressure was normal and a small amount of air was ducted through the port in the model base, the vortices were filled with air, and again became visible (Fig. 5). An increase in the air-flow rate produced a short, frothy cavity (Fig. 6); a further increase formed a full, smooth cavity that extended several chord-lengths downstream (Fig. 7).

An interesting and important aspect of these tests is that the air did not spring forward to the leading edge unless the angle of attack was increased to about 13^{o}; at this angle the fully wetted hydrofoil normally stalled (Fig. 8). Alternatively, if the static pressure was sufficiently low, a patch of vapor cavitation extended rearward from the leading edge and eventually combined with the air cavity at the base. Figure 9 shows the hydrofoil with vapor cavitation at the leading edge and a full air cavity at the base; no photographs are available showing the union of these two cavities. Occasionally, a thin wisp of ventilation was seen on the upper surface in the region just ahead of the base (Fig. 10), but it was found to have only a small effect on the lift and drag. This phenomenon is believed to have been caused by ventilation of a thin layer of separated boundary-layer water on the upper surface near the base. Futher evidence of upper-surface separation is shown in Fig. 11, where patches of air are seen behind the base and above the trailing air cavity, indicating that air has ventilated from the cavity into the vortices of the separated flow. Another interesting flow phenomenon occurred in the tests of the model having an aspect ratio of 1.44. Figure 12 shows this model with fully developed base ventilation; note the three-dimensional pattern behind the base at the outer tip (clearly visible in the upper picture) caused by ventilation of the tip vortex. Also of interest is the fact, revealed by these photographs, that the hydrofoil tip did not ventilate forward of the base.

As the air-flow rate was decreased from a large value, the cavity remained smooth and long, but became more and more unstable, until finally any slight change in the air-flow rate (increase

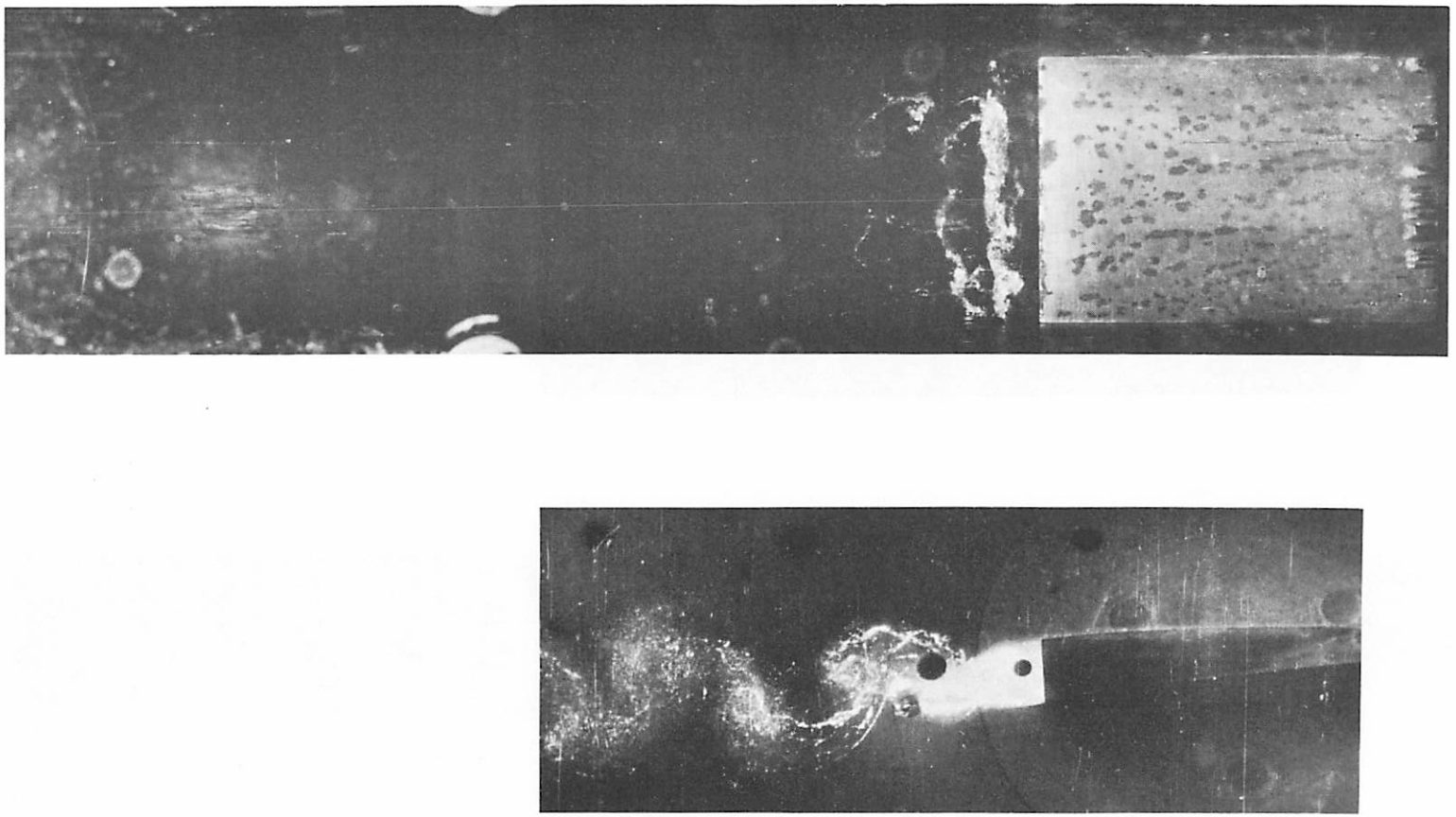

FIG. 4. Vapor Cavitation at Base of Hydrofoil. Q' = 0, $\alpha = 4^{o}$, $\mathcal{R} = \infty$. Base cavitation began at $\sigma = 2.30$, photograph taken at $\sigma = 1.04$.

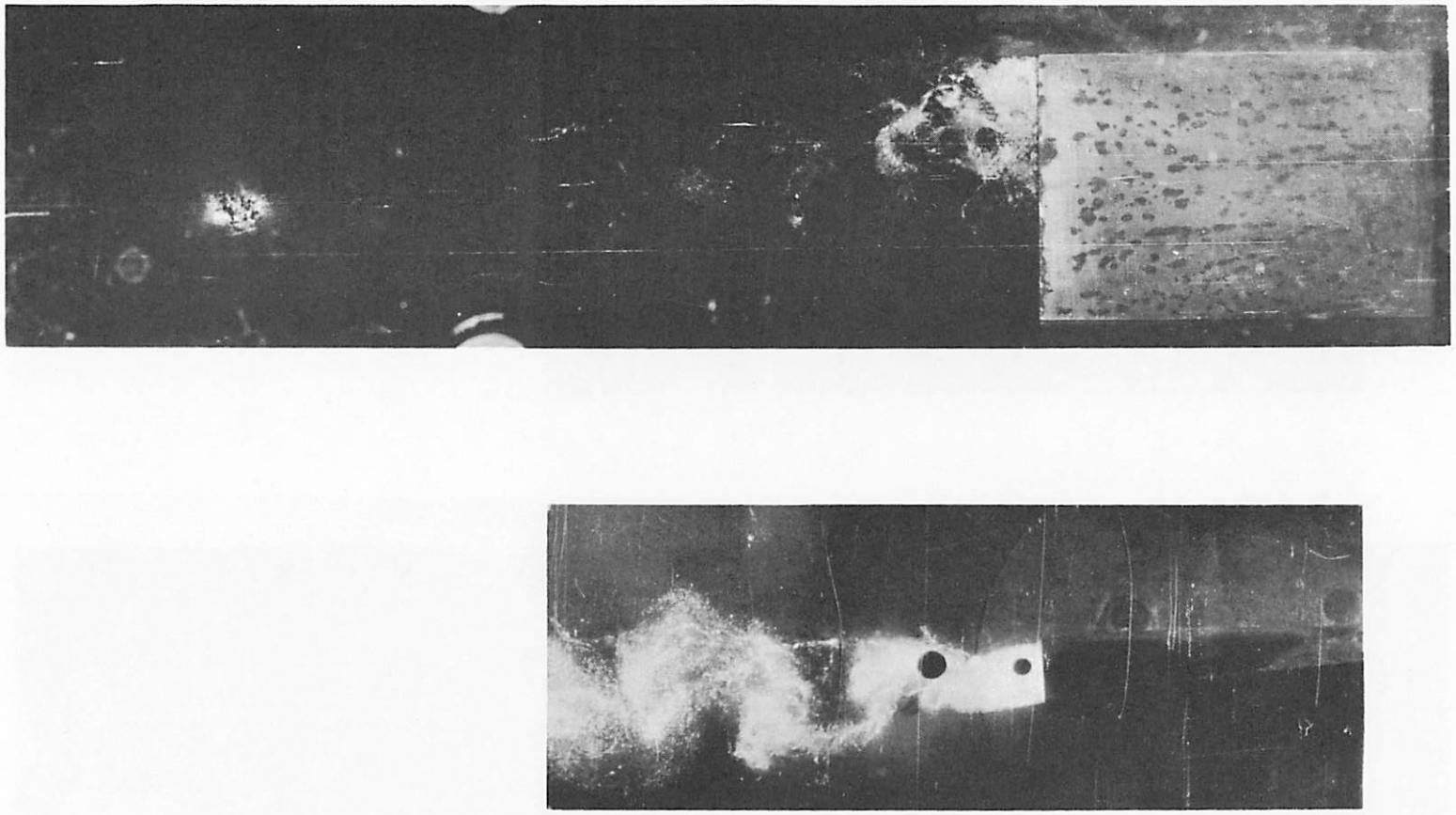

FIG. 5. A Very Small Air-Flow Rate. $Q' = 0.004$, $\sigma = 4^{o}$, $AR = \infty$. K, not measured, is between 0.3 and 0.5.

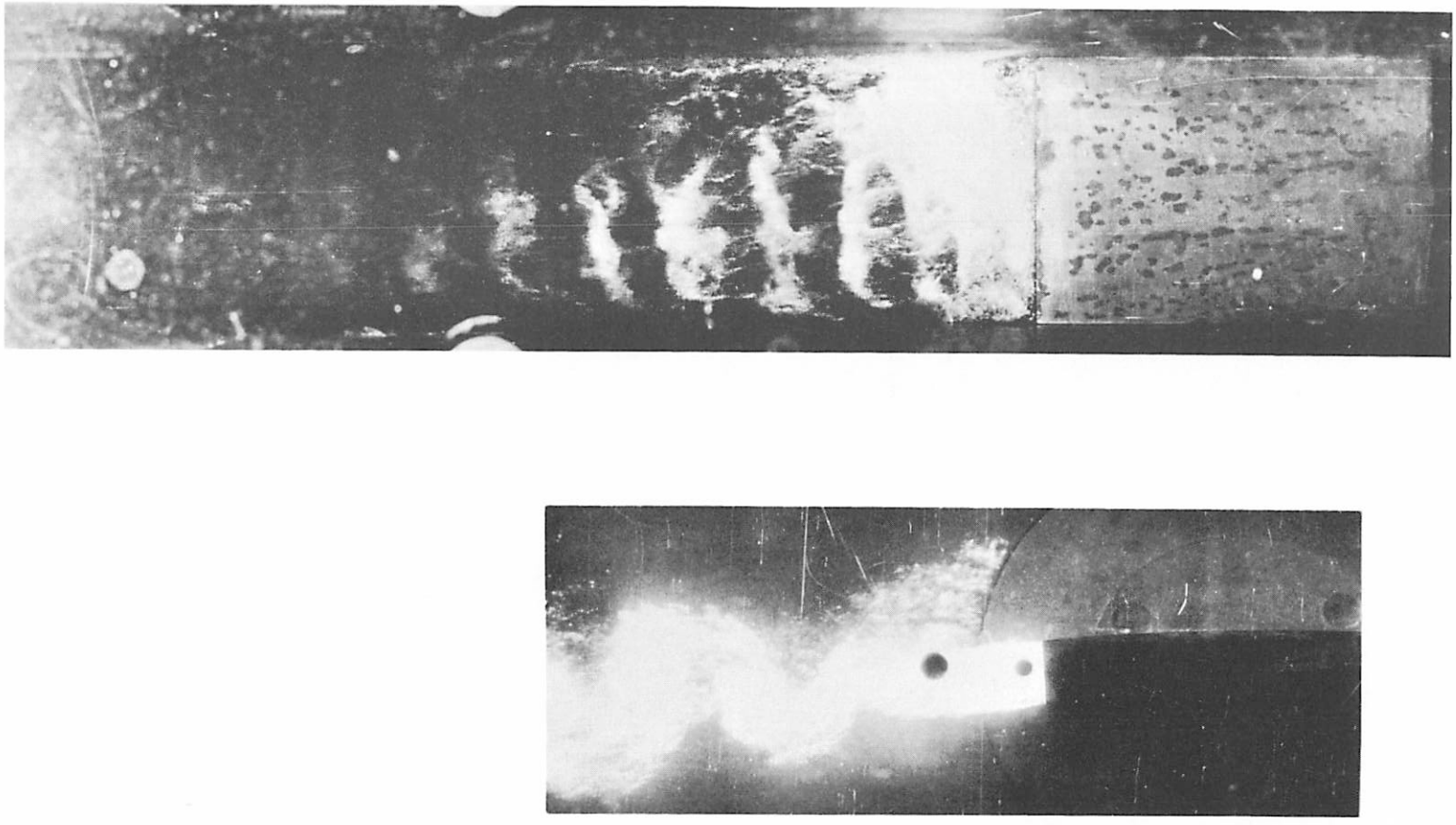

FIG. 6. A Short Cavity. $Q' = 0.024$, $\alpha = 4^{o}$, $AR = \infty$. K, not measured, is between 0.3 and 0.5.

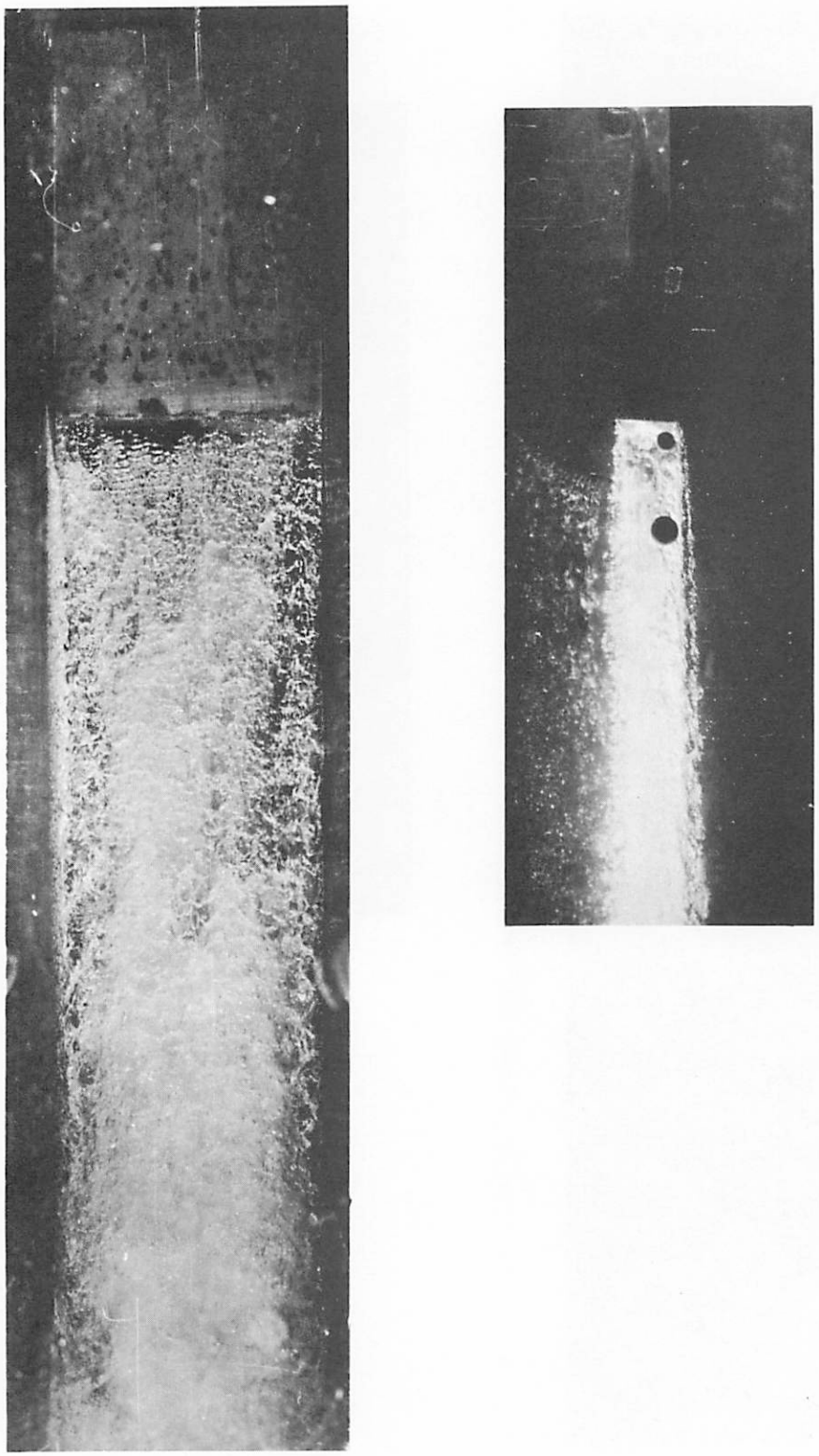

FIG. 7. A Full Cavity. $K = 0.139$, $Q' = 0.076$, $\alpha = -2^{\circ}$, $AR = \infty$.

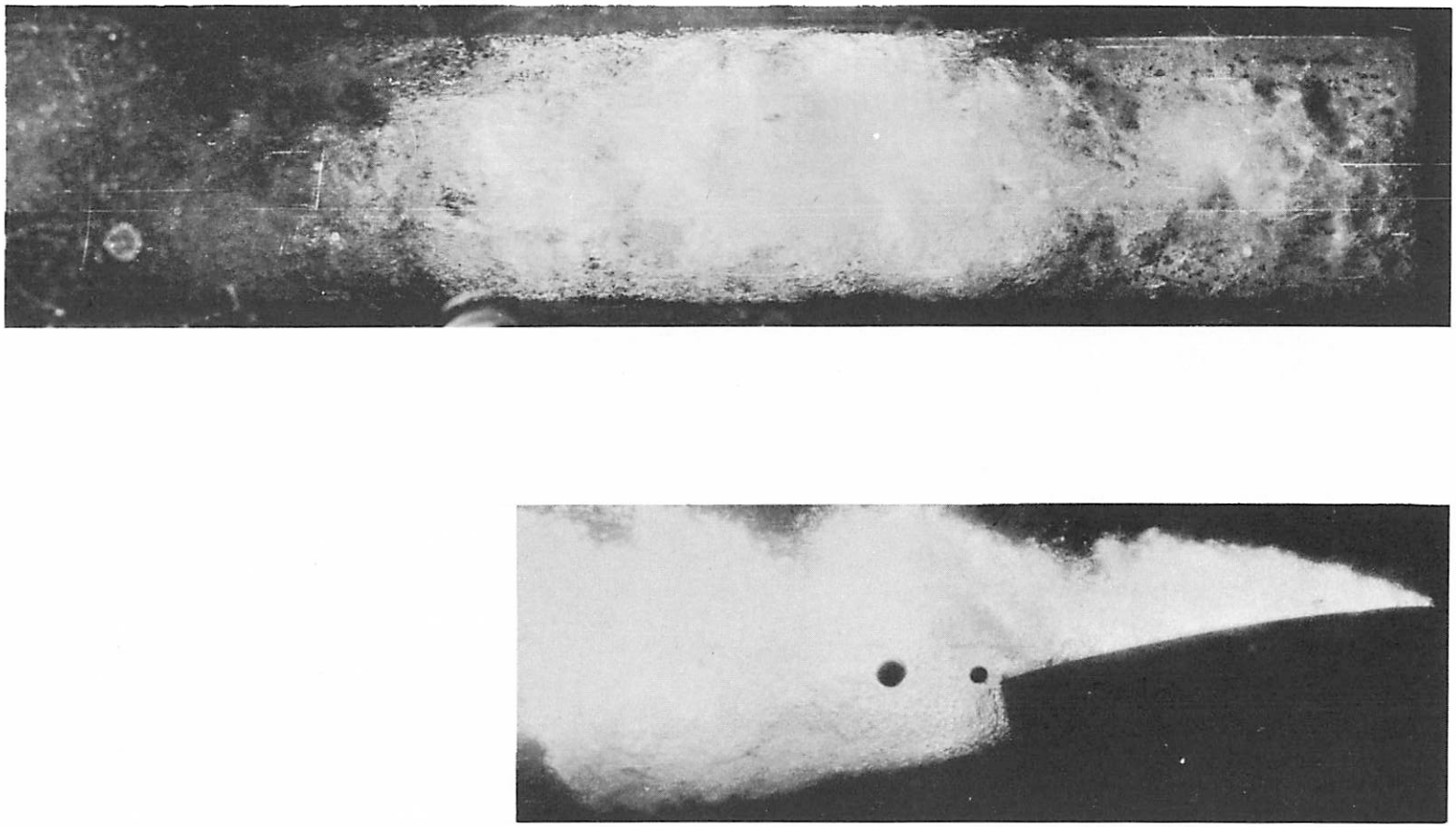

FIG. 8. Stalling Point With a Full Cavity. $K = 0.532$, $Q' = 0.209$, $\alpha = 14^{o}$, $AR = \infty$.

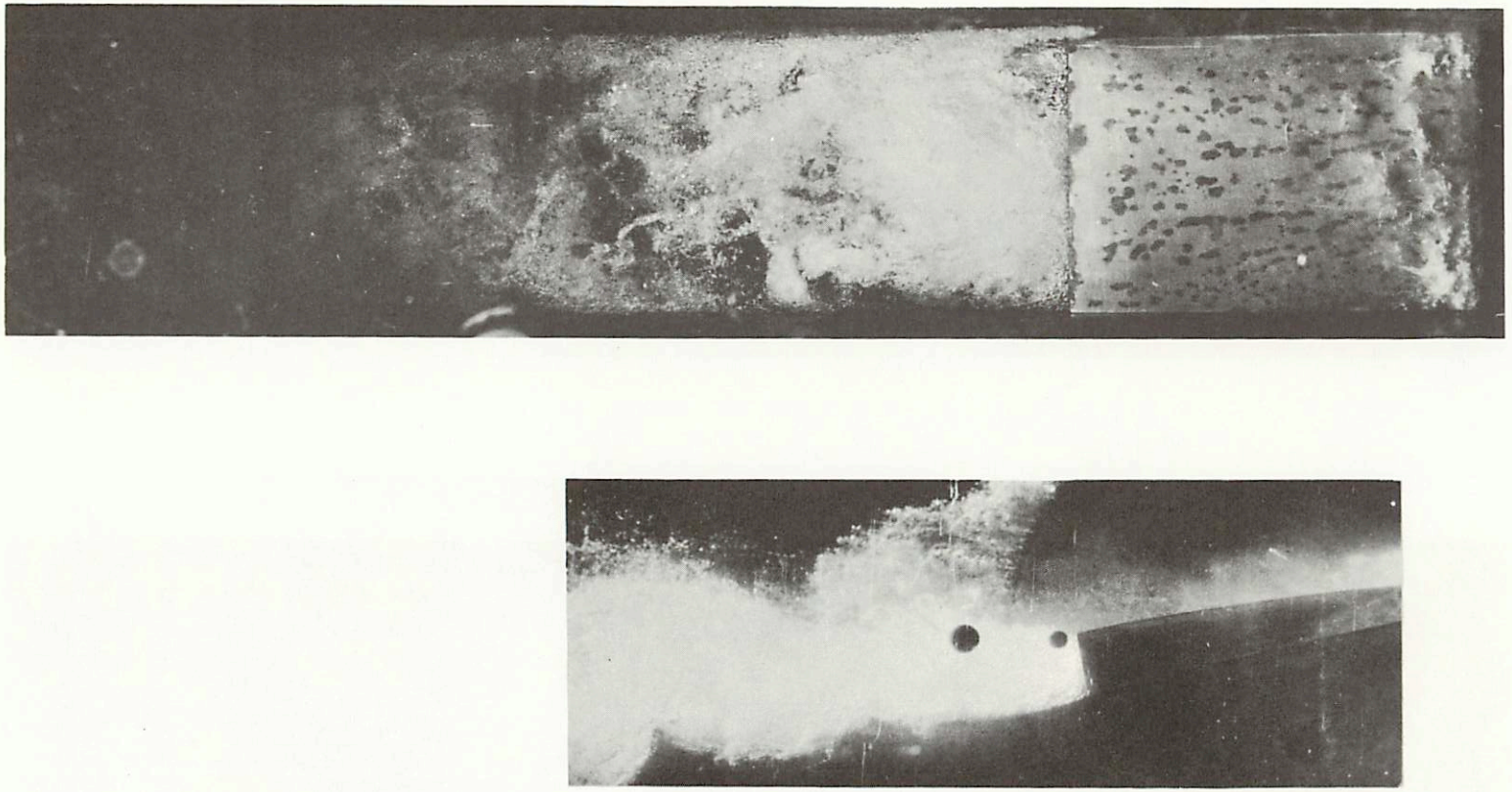

FIG. 9. Vapor Cavitation at Leading Edge. K = 0.261, Q' = 0.082, $\alpha = 10^{\circ}$, $\sigma = 2.55$.

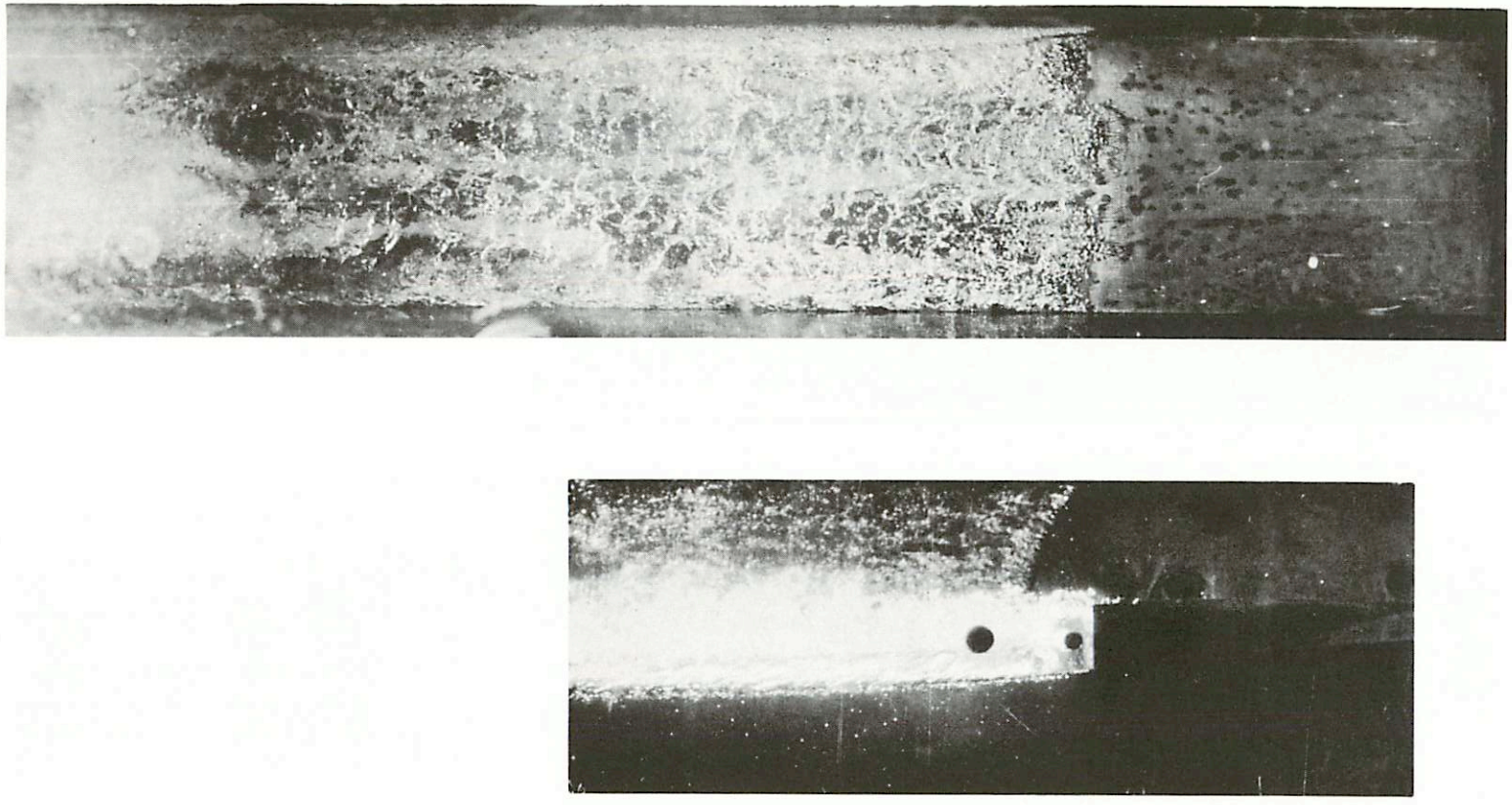

FIG. 10. Ventilation of Boundary Layer at Trailing Edge.
K = 0.146, Q' = 0.095, $\alpha = 2^{o}$, AR = ∞.

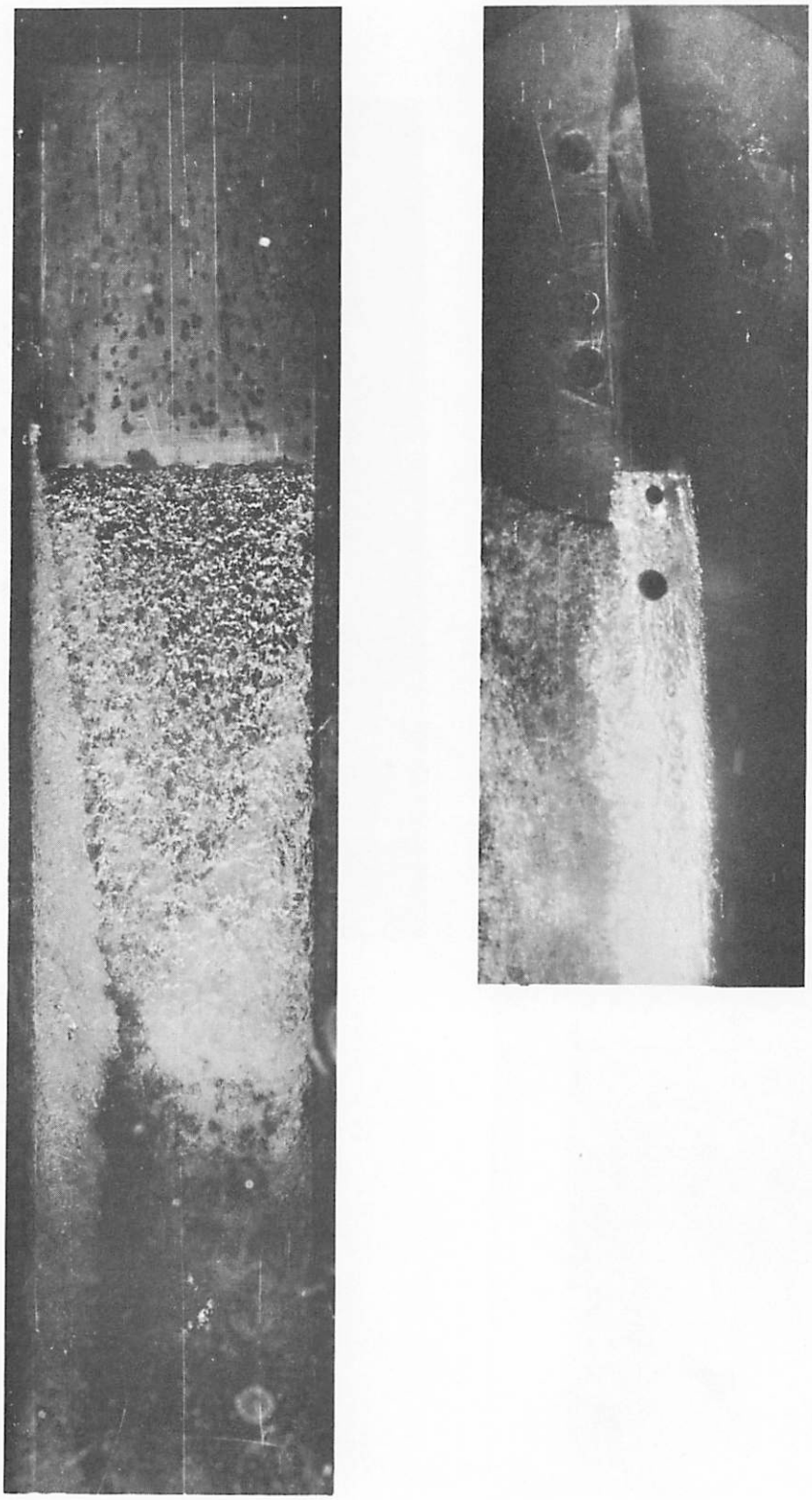

FIG. 11. Ventilation of Separated Region Above Cavity.
$K = 0.146$, $Q' = 0.089$, $\alpha = 4^{\circ}$, $AR = \infty$.

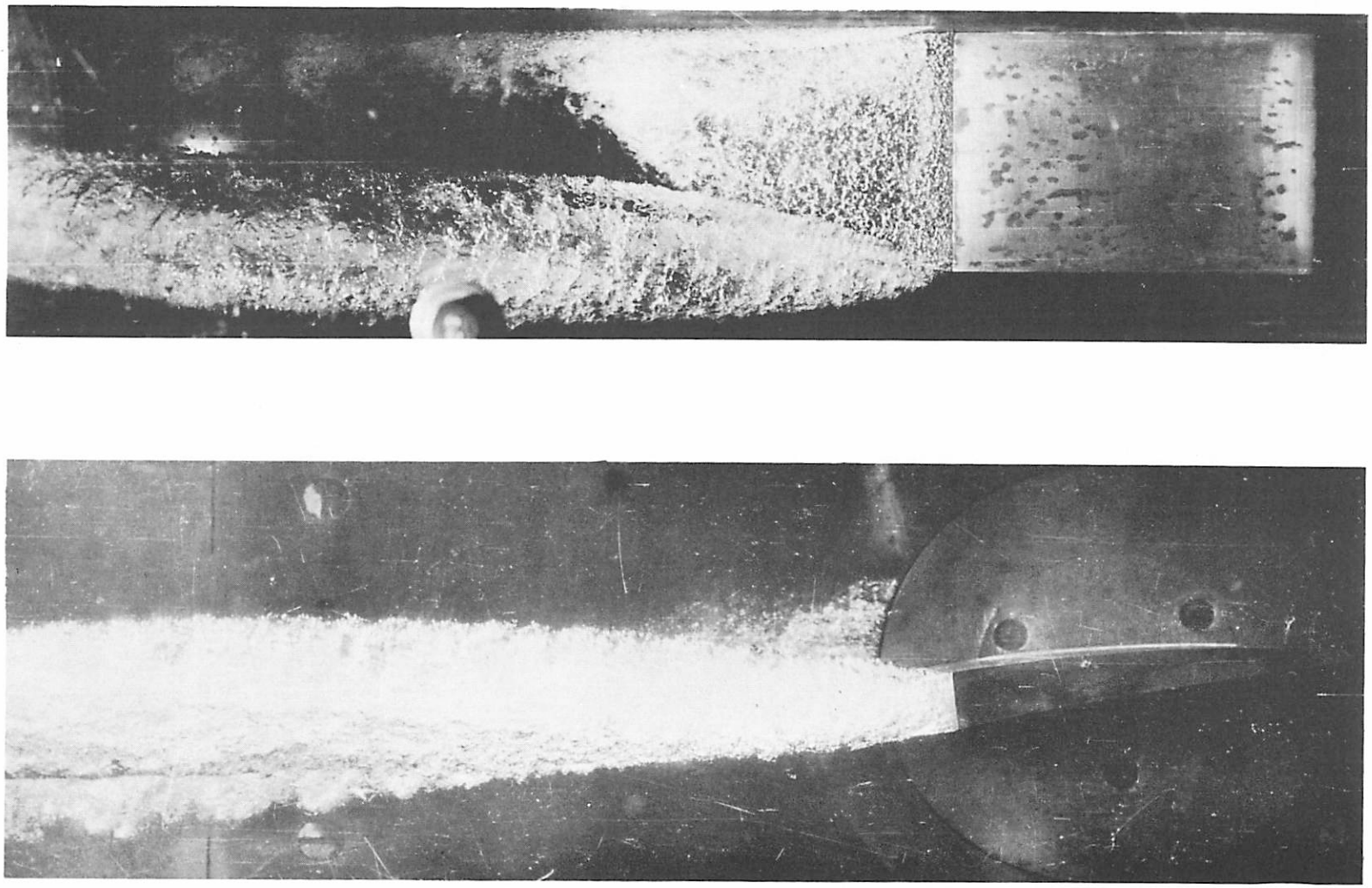

FIG. 12. A Full Cavity With a Finite Aspect Ratio. K = 0.100, Q' = 0.071, $\alpha = 8^{o}$, AR = 1.44.

or decrease) caused the sudden collapse of the cavity back to the short, frothy type. Thus, at an intermediate air-flow rate, the cavity can be of either type. In the upper photograph of Fig. 13 the cavity is long and smooth; a very slight decrease in air-flow rate changes it to the frothy type shown in the lower photograph. This sudden change in the cavity occurred only with the finite-aspect-ratio hydrofoil. In the infinite-aspect-ratio tests the cavity became gradually shorter and more frothy as the air-flow rate decreased.

BASE PRESSURE

The pressure in the region behind the base of the hydrofoil is important in determining the drag. It was found to be a function of the rate of air flow into this region and designated by a convenient nondimensional pressure coefficient, the ventilation number K.

$$K = \frac{P_\infty - P_c}{q_\infty}$$

where P_∞ and q_∞ are the static pressure and dynamic pressure upstream of the model, and P_c is the base (or cavity) pressure. A nondimensional air-flow-rate coefficient Q' is defined as

$$Q' = \frac{Q}{bt\,V_\infty}$$

where Q = air-flow rate, b = hydrofoil span, and t = hydrofoil base thickness.

When the hydrofoil with infinite aspect ratio is fully wetted, K = 0.50 (Fig. 14). As air is injected into the base region, K decreases rapidly with increasing Q', and approaches an asymptotic value of 0.13 as Q' reaches 0.07. An increase in Q' beyond 0.07 produces no significant change in K. In previous experiments on streamlined hydrofoils with ventilation through the surface (Ref. 3), it was found that the forces and the ventilation number began to level off at the same value, Q' = 0.07. (In these experiments, t was defined as the height of the projection, in the free-stream direction, of the air-covered surface of the hydrofoil.) Therefore, this value of Q' = 0.07 appears to be general since it remains essentially unchanged with respect to model shape and angle of attack. Both series of tests were conducted in the High-Speed Water Tunnel at CIT, however, and the wall-interference effects may have influenced this value. The asymptotic minimum value of K = 0.13 is definitely due to tunnel-wall

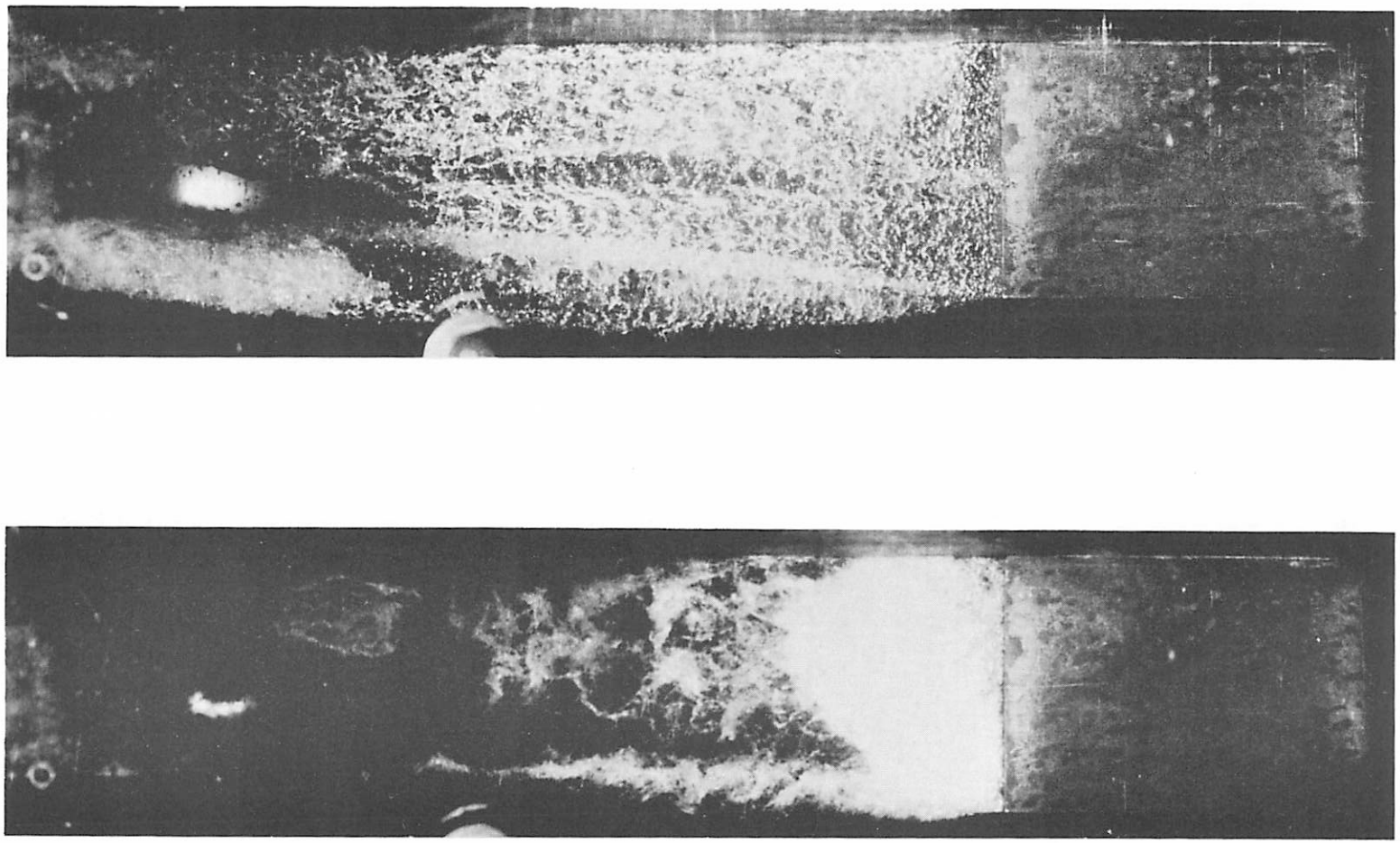

FIG. 13. The Two Types of Cavity Possible at an Intermediate Air-Flow Rate. Upper photograph: long, smooth cavity, $Q' = 0.035$, $K = 0.064$, $\alpha = 2^{\circ}$. Lower photograph: short, frothy cavity, $Q' = 0.033$, $K = 0.196$, $\alpha = 2^{\circ}$. $AR = 1.44$ in both photographs.

interference; and it is in fair agreement with the theoretical value of $K_{min} = 0.16$ calculated in Appendix B, using the tunnel-blockage theory.

One side-plate in the tunnel was removed to reduce the hydrofoil aspect ratio to 1.44. Figure 15 shows that for this model $K = 0.36$ in fully wetted flow, and that it approaches an asymptotic minimum of $K = 0.06$ as the air-flow rate Q' is increased. As in the infinite aspect ratio case, a critical air-flow rate of $Q' \cong 0.07$ was observed. The minimum value of $K = 0.06$ is lower than that for the infinite-aspect-ratio model because of the reduction in tunnel blockage caused by removing one side-plate. This minimum value is in fair agreement with the theoretical value $K_{min} = 0.08$ calculated in Appendix B. Most of the data in Fig. 15 were taken as Q' was decreased. In the intermediate range of air-flow rates, $0.03 < Q' < 0.08$, the jump in cavity pressures is a result of the sudden change from a long, smooth cavity to a short, frothy cavity.

LIFT COEFFICIENT

The model used for this experiment has an NACA $a = 1.0$ camber line which is designed for a lift coefficient $C_{L_d} = 0.40$ ($= C_{L_o}$) at $\alpha = 0^o$, when $AR = \infty$. The experimental lift data are plotted in Fig. 16, showing (for $AR = \infty$ and $\alpha = 0^o$) that $C_{L_o} = 0.25$, fully wetted, and $C_{L_o} = 0.20$, base vented. The experimental values of C_{L_o} are thus only 50 to 60% of the theoretical value; the experimental lift coefficient derivative C_{L_α} is only 5.50, instead of the theoretical value 6.28. A lower lift coefficient than the theoretical one has been observed before in wind-tunnel tests of airfoils having the same NACA $a = 1.0$ camber line. Reference 6 reports that airfoils having this camber line and a theoretical $C_{L_o} = 0.40$, show an experimental C_{L_o} between 0.25 and 0.33 and a C_{L_α} between 5.7 and 6.8. The experimental results for other types of camber lines, such as the circular arc, agree more closely with theory. The experimental lift coefficient of the cambered parabola is thus in fair agreement with those of streamlined airfoils having the same camber line.

The $a = 1.0$ camber line theoretically provides a uniform chordwise loading which, by definition, has a pressure discontinuity at the leading and trailing edges. Physically this pressure change must be distributed over a finite distance. At the base, for instance, the static pressures on the upper and lower surfaces must both be equal to the cavity pressure; therefore, the pressure on these surfaces near the base must be altered from theory. Such pressure alteration would probably tend to change the pressure

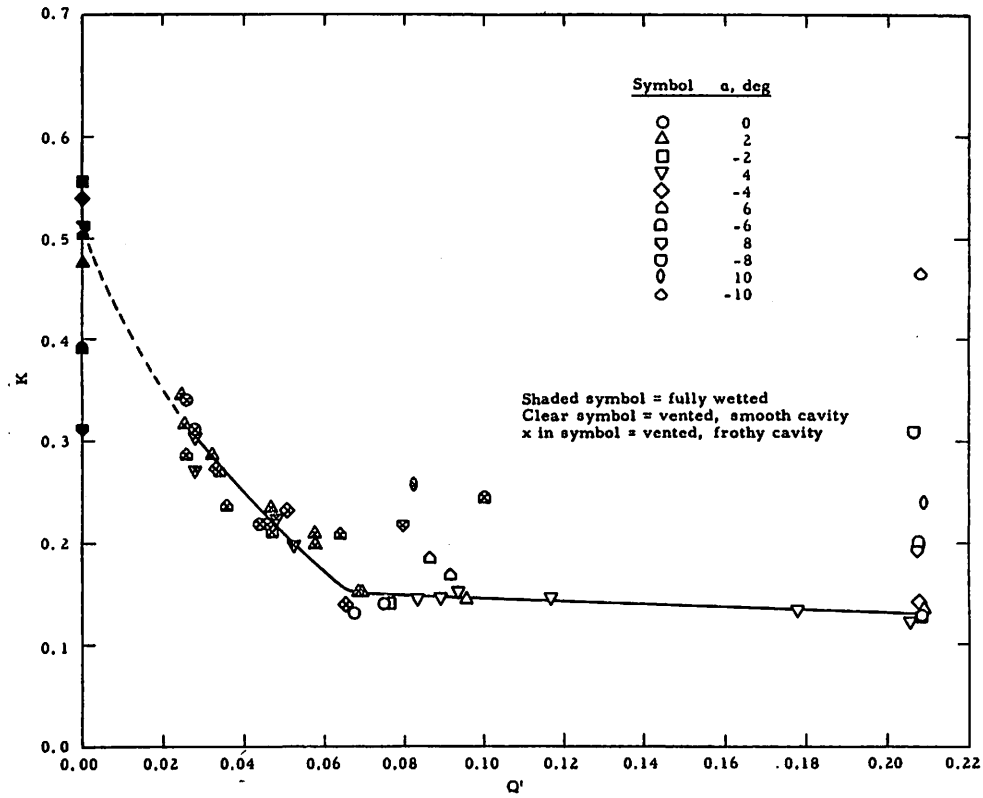

FIG. 14. K Versus Q' With AR = ∞.

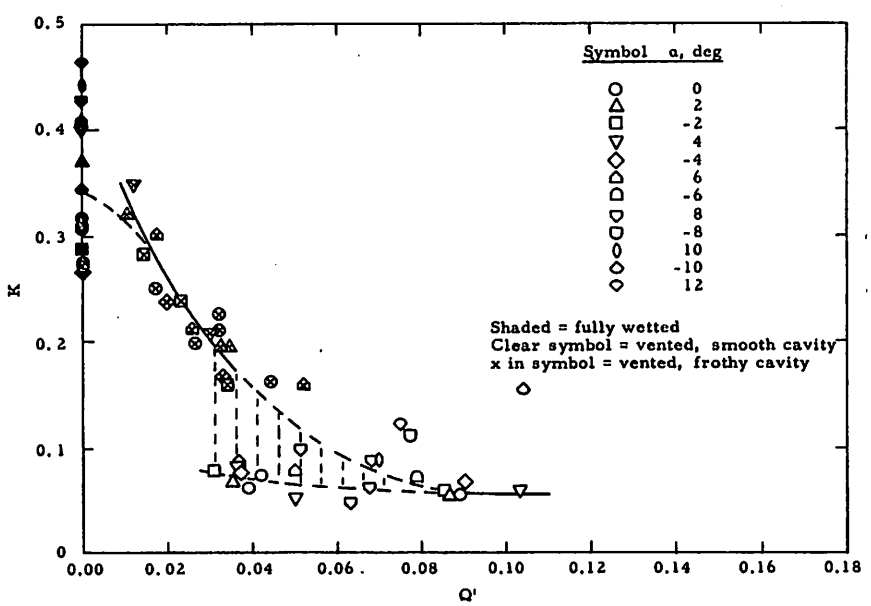

FIG. 15. K Versus Q' With AR = 1.44.

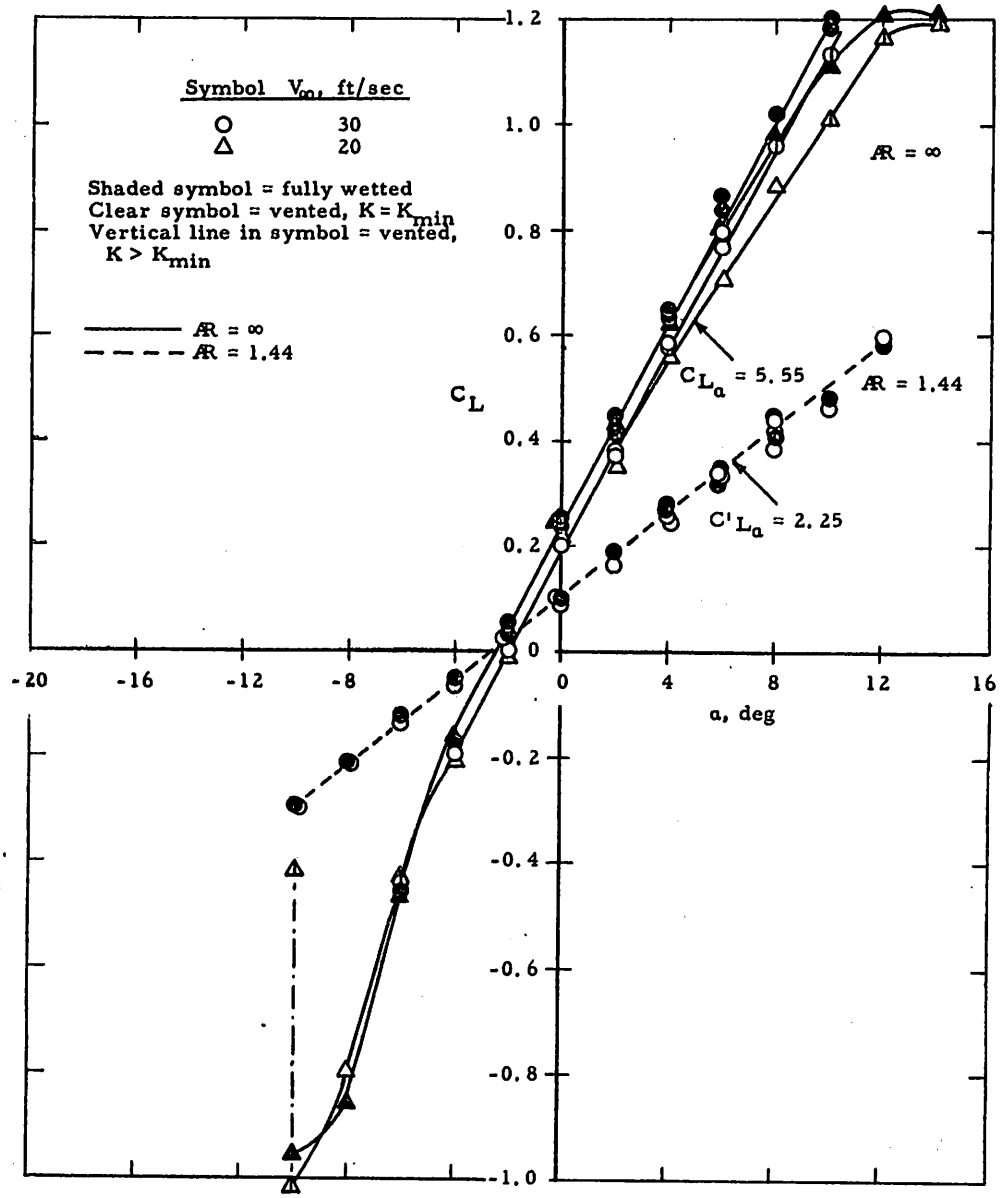

FIG. 16. C_L Versus α With AR = ∞ and AR = 1.44.

distribution near the base to something more similar to that of the NACA a = 0.8 or a = 0.9 camber lines and near the leading edge to something more like the 16-series airfoils. If the pressure gradient on the upper surface near the base is unfavorable (i.e., pressure increases in the direction of flow), the boundary layer will tend to separate. Remembering that the theoretical pressure coefficient on the upper surface of the model is $-(C_{L_d}/2) = -0.20$, the boundary layer can separate when the ventilation number K is less than 0.20. Evidence of boundary-layer separation is seen in Fig. 10 and 11 where the air has ventilated into the separated-flow region. The sudden appearance of this separation and its effect on the lift is seen in Fig. 17, where C_L is plotted as a function of K for various angles of attack. C_L remains nearly constant as K decreases from the fully wetted value of 0.5 toward 0.20, and then C_L drops by 0.03 to 0.11. In general, this change in C_L is relatively small, but significant.

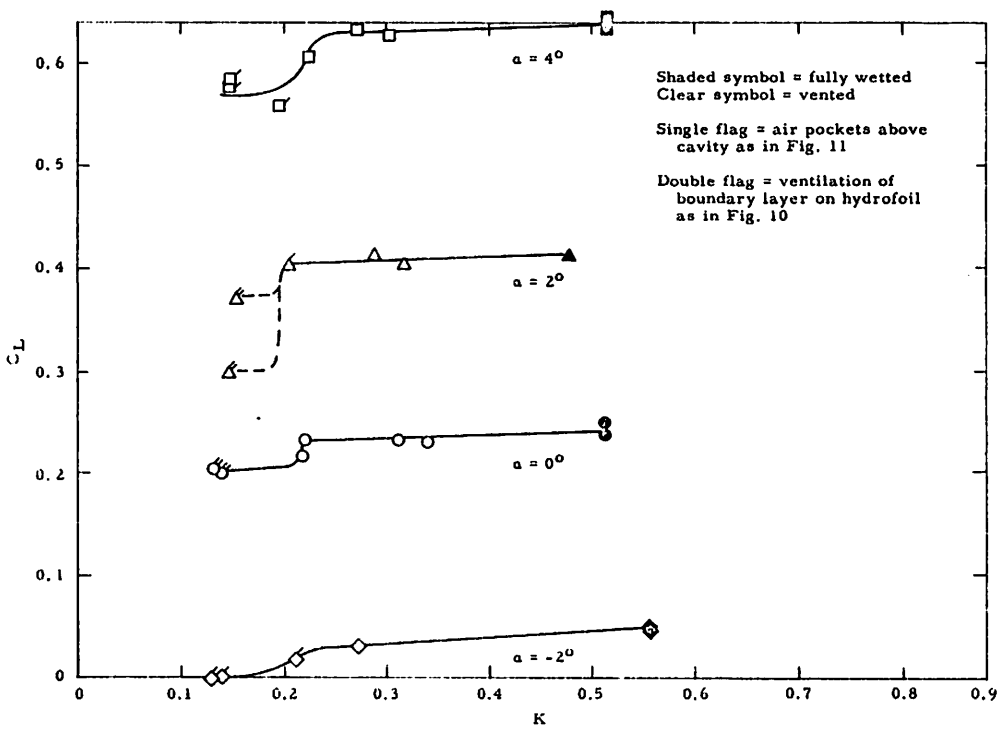

FIG. 17. C_L Versus K With $\mathfrak{R} = \infty$.

The experimental results plotted in Fig. 16, for $\mathfrak{R} = 1.44$, show a value of $C_{L_o} = 0.10$, fully wetted, and 0.09, base vented. The lift coefficient derivatives are both 2.25. A theory for

low-aspect-ratio wings developed by H. B. Helmbold and reported in Ref. 9 shows that

$$C'_{L_\alpha} = \frac{C_{L_\alpha}}{\frac{C_{L_\alpha}}{\pi AR} + \sqrt{1 + \frac{4}{AR^2}}}$$

Using the equation

$$C'_{L_o} = \frac{C'_{L_\alpha}}{C_{L_\alpha}} C_{L_o}$$

and assuming $C_{L_o} = 0.40$, it is seen that, in theory,

$$C'_{L_o} = 0.13 \text{ and } C'_{L_\alpha} = 2.07 \text{ for } AR = 1.44 + 0.04 = 1.48$$

where 0.04 is a correction for the square tip of the hydrofoil (Ref. 10). As in the case of the infinite aspect ratio, the experimental lift coefficient is lower than the theoretical value. The experimental lift coefficient derivative, however, is about 10% higher than in theory, whereas in the test with $AR = \infty$ the C_{L_α} was about 12% lower.

The curve of C_L versus α in Fig. 16 shows that the lift coefficient is linear from $\alpha = -4^o$ to $\alpha = +10^o$ for both aspect ratios. The upper stall occurs at 12 to 13°. A peculiar slope change appears in the C_L curve for $AR = \infty$ at $\alpha = -4^o$ that may be due to laminar separation on the lower surface near the leading edge. The negative stall angle is about -10°. A velocity scaling effect is noticeable at angles of attack greater than $\alpha = 2^o$; when $V_\infty \cong 20$ ft/sec, the lift curve is lower than when $V_\infty \cong 30$ ft/sec, for both the fully wetted and the base-vented cases. No scaling effect is noticeable around $\alpha = 0^o$ or at the negative angles of attack.

Johnson and Rosnick (Ref. 11) present results of recent NASA experiments, in the Langley Towing Tank, with a cambered hydrofoil having a parabolic thickness distribution. The NASA hydrofoil model had an aspect ratio of 1.0 and was tested at speeds in the range of 100 knots. The hydrofoil was cambered to a design lift coefficient of 0.28, using the NACA a = 1.0 camber line. Results of the NASA tests showed that $C'_{L_o} = 0.04$ and $C'_{L_\alpha} = 1.8$. These results are in fair agreement with the experimental data reported here since this value of C'_{L_o} was about 40% less than

the theoretical value of 0.067 and C'_{L_α} was 20% greater than the theoretical value of 1.5, as obtained from the theory of H. B. Helmbold.

MOMENT COEFFICIENT

The moment coefficient is plotted as a function of α for $\mathcal{AR} = \infty$ and $\mathcal{AR} = 1.44$ in Fig. 18 and 19, respectively. The moment coefficient C_{M_0} for $\mathcal{AR} = \infty$ is -0.080 when fully wetted and -0.065 when base vented at minimum K. The experimental values of C_{M_0} for airfoils having the a = 1.0 camber line, $\mathcal{AR} = \infty$, and a theoretical $C_{L_0} = 0.40$ are shown by Ref. 6 to lie between -0.067 and -0.082. (The theoretical values of C_{M_0} for the NACA a = 1.0 and a = 0.8 camber lines are -0.10 and -0.08, respectively.) When $\mathcal{AR} = 1.44$, the experimental values of C_{M_0} are -0.060 and -0.055 for the wetted and vented cases, respectively. The moment coefficient derivatives C_{M_α} are -0.14 and -0.02 for aspect ratios of ∞ and 1.44, indicating that the hydrodynamic center (center of pressure of the force resulting from changes in α) is at the 27.5% and 26% chord-points, respectively, aft of the leading edge. These results are in fair agreement with the theoretical values, for a fully wetted flat plate, of 25% for $\mathcal{AR} = \infty$ and 20% for $\mathcal{AR} = 1.44$.

DRAG COEFFICIENT

The drag of a base-vented hydrofoil is composed of frictional drag, cavity drag, separation drag, and, for finite aspect ratios, induced drag and tip drag. These components are expressed in the following equation:

$$C_D = C_{D_f} + C_{D_c} + C_{D_s} + C_{D_i} + C_{D_t} = \frac{\text{Drag}}{q_\infty A}$$

The frictional drag coefficient is a function of Reynolds number R_c, cross-sectional shape, and angle of attack, since they all influence the state of the boundary layer. The boundary-layer state was not determined in these experiments, but it was believed to be turbulent because of the relatively high turbulence level in the water of the tunnel. If the boundary layer were entirely turbulent, C_{D_f} would be about 0.0090, corresponding to $R_c = 9 \times 10^5$ at $V_\infty = 30$ ft/sec.

The cavity drag is a function of the hydrofoil cross-sectional shape and the ventilation number of the cavity, or wake, formed behind the base. Theoretically, the cavity drag of an uncambered

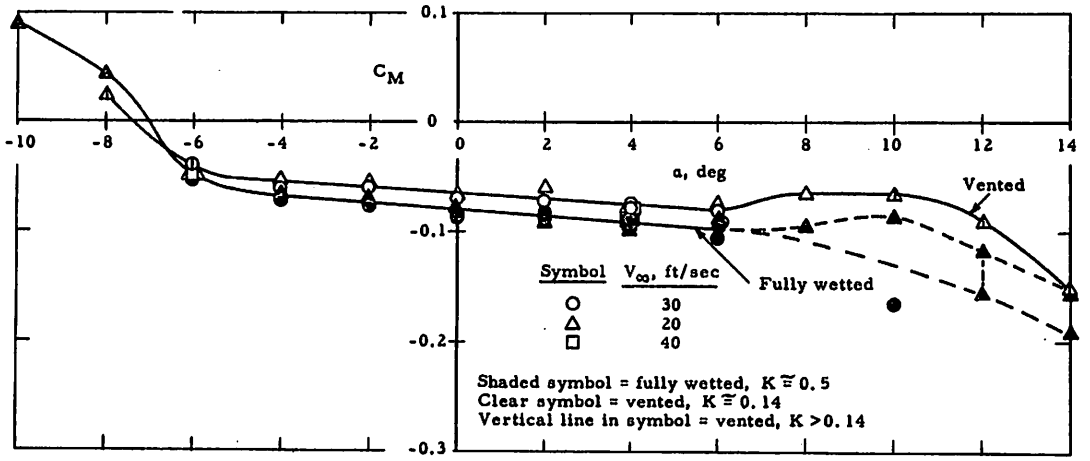

FIG. 18. C_M (About Quarter Chord) Versus α With AR = ∞.

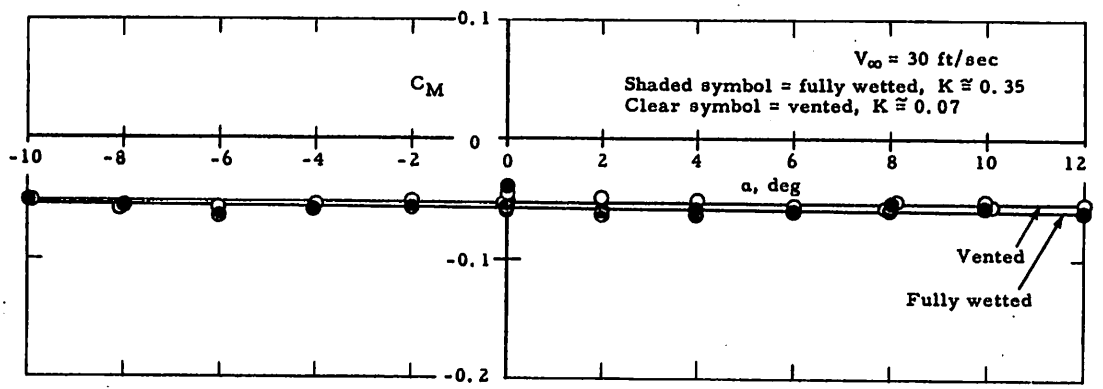

FIG. 19. C_M (About Quarter Chord) Versus α With AR = 1.44.

or a cambered parabolic cross section having a base-thickness-to-chord ratio τ, is

$$C_{D_c} = \frac{\pi}{8} \tau^2 + f(K)$$

where

$$K = \frac{P_\infty - P_c}{q_\infty} = \text{ventilation number}$$

The relatively complex term f(K) is defined as zero when K = 0. Methods for evaluating C_{D_c} are presented by Wu (Ref. 12), Tulin (Ref. 13), and Fabula (Ref. 14). By definition, K = 0 when $P_c = P_\infty$ = static depth pressure, and K > 0 when $P_c < P_\infty$. Therefore, as K increases, the pressure behind the base decreases and consequently the cavity drag increases.

The separation drag is caused by pressure drag on the hydrofoil, resulting from boundary-layer separation on the upper or lower surface ahead of the base. The separation drag is defined as the increase beyond the minimum drag for $\mathrm{AR} = \infty$, resulting from changes in angle of attack. It is a relatively complex function of airfoil shape, surface smoothness, Reynolds number, tunnel turbulence, and $(\alpha - \alpha_m)$, where α_m is the angle of attack at which the minimum drag is measured. Theoretically, α_m is equal to the design angle of attack α_d at which the design pressure distribution occurs. In practice this is generally not true since α_m is affected by surface roughness and Reynolds number. For very smooth airfoils, having a turbulent boundary layer and a thickness-to-chord ratio of 15% (NACA 2415 and 4415), Ref. 6 shows that the value of C_{D_s} is close to zero for α in the range of $\alpha_m \pm 5^\circ$ and increases rapidly as α leaves this range. The drag data obtained from the experiments reported here for $\mathrm{AR} = \infty$ are plotted in Fig. 20 and show essentially the same trend. The minimum drag coefficient occurs around $\alpha = 1.3^\circ = \alpha_m$. This result is in fair agreement with airfoil data reported in Ref. 6 where α_m varied from 0.3 to 1.0°.

The induced drag exists only on hydrofoils having a finite aspect ratio, and it is caused by the downwash induced by lift. For an elliptical planform the theoretical induced drag is $C_{D_i} = C_L^2/\pi \mathrm{AR}$. The induced drag is a few percent higher for a rectangular planform. Figure 21 shows C_D versus α for AR = 1.44, plotted for three different experimental values of K. The curves look similar to those for $\mathrm{AR} = \infty$ except that they exhibit a much larger dependence on α, particularly at the lower angles of attack. This increased dependence is caused by the induced drag.

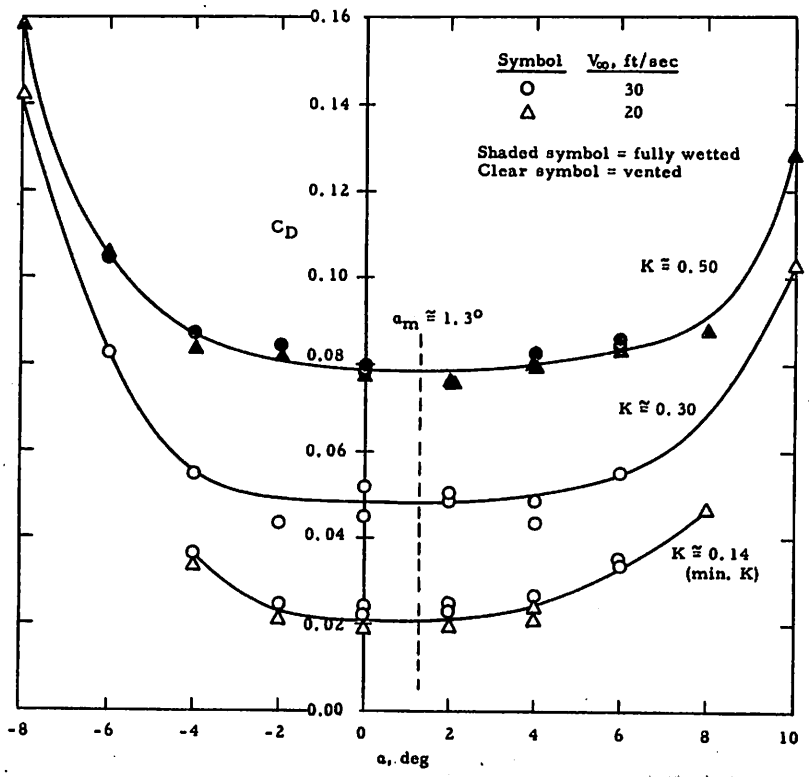

FIG. 20. C_D Versus α With $\mathfrak{R} = \infty$.

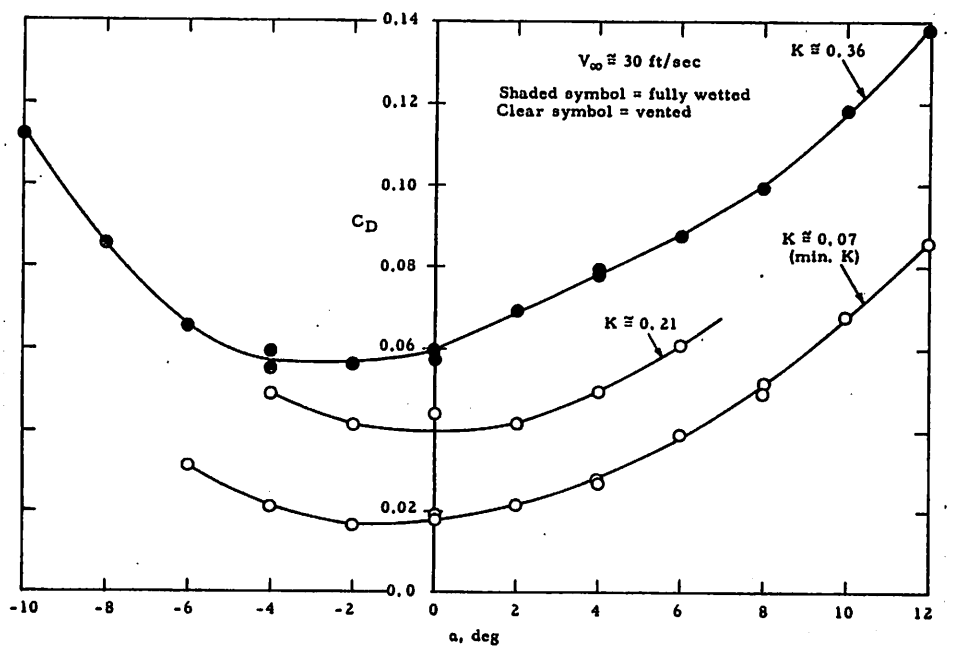

FIG. 21. C_D Versus α With $\mathfrak{R} = 1.44$.

If it is assumed that the separation drag remains constant and independent of aspect ratio, and that the frictional drag, cavity drag, tip drag, and tunnel-interference effects are independent of α for small values of α, it is possible to obtain the experimental induced drag from Fig. 20 and 21. To do this, the curves of C_D versus α in Fig. 20 for $AR = \infty$ and in Fig. 21 for $AR = 1.44$ are shifted downward until they are tangent to the $C_D = 0$ line. (This eliminates frictional drag, tip drag, and cavity drag.) Then an average curve is drawn for each aspect ratio, and is replotted versus C_L (Fig. 22). The curve for $AR = \infty$ is the separation drag C_{D_s}. The dashed line is the curve for $AR = 1.44$, C_D^*. It should be noted that some separation drag already exists at the minimum point on the C_D^* curve; this curve therefore represents the induced drag C_{D_i} for $AR = 1.44$, plus the separation drag C_{D_s}, minus the separation drag at $C_L = 0$, $C_{D_{s(o)}}$. The value of the induced drag C_{D_i} is obtained from these two curves and is also plotted in Fig. 22.

The resulting experimental induced drag is

$$C_{D_{i(exp)}} \cong 1.2 \frac{C_L^2}{\pi AR} \text{ for } C_L > 0$$

$$C_{D_{i(exp)}} \cong 2.4 \frac{C_L^2}{\pi AR} \text{ for } C_L < 0$$

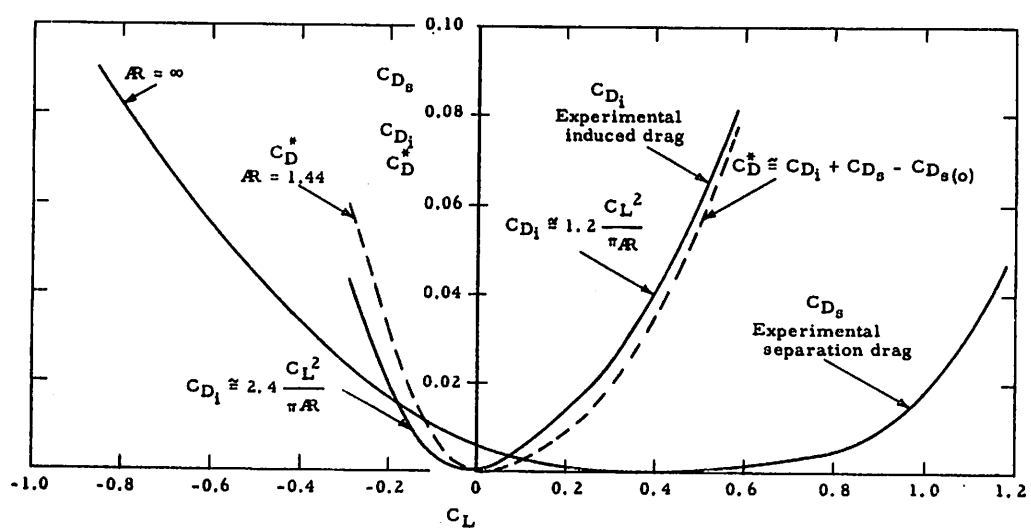

FIG. 22. Experimental Separation Drag and Induced Drag.

The induced drag coefficient for $C_L > 0$ is in fairly good agreement with theory. The large disagreement with theory when $C_L < 0$ may be due to the fact that an interaction occurs between the induced and separation drags, so they cannot be subtracted algebraically. Since the separation drag was near zero for $C_L > 0$, there was no such interaction in that range.

The drag due to the blunt tip of the finite-aspect-ratio hydrofoil has been estimated using an empirical equation from Hoerner (Ref. 10):

$$C_{D_t} = 0.104 \left(\frac{t}{c} \right)^2 = 0.0023$$

Although Hoerner derived his equation from data on square-tipped wings with streamlined cross sections, it is assumed to be approximately correct for the cross section tested here.

The effect of ventilation number K on drag is seen in Fig. 23 and 24. Although the experimental data are somewhat scattered, they show that the drag coefficient $D' = \text{Drag}/q_\infty A_b$ is directly proportional to K at all angles of attack for both $AR = \infty$ and $AR = 1.44$. This result indicates that those portions of drag that are due to changes in angle of attack, such as the separation drag and the induced drag, remain constant and independent of ventilation number and hence of cavity drag.

Figure 25 shows D' plotted as a function of K for $\alpha = 0^\circ$ with $AR = \infty$. This graph also includes the tunnel-wall-interference corrections which were applied to the drag data, and two theoretical curves of D' versus K. The corrections in drag due to the spindle disk, tunnel blockage, and horizontal buoyancy are small but significant. These corrections are discussed in Appendix B. As mentioned previously, D' varies directly as K. The dimensional drag D therefore increases directly as the base pressure decreases. This trend agrees in general with that predicted by the linearized cavity theories (Ref. 12 and 14). The theoretical curves shown in Fig. 25 were taken from Ref. 14. They show cavity drag coefficient versus K for the closed-cavity model and for the open-cavity model, in which the cavity is followed by a wake of maximum thickness. Partly closed cavities, with wake thicknesses lower than that of the open-cavity model, would give drag values lying between these two curves. The open-cavity drag curve quickly approaches the line $D' = K$, its asymptote for large K. The difference between the corrected experimental drag curve and the theoretical drag curves presumably represents the frictional drag, since the induced and separation drags are zero at $\alpha = 0^\circ$. The difference is $\Delta D' = 0.016$ for the open-cavity curve

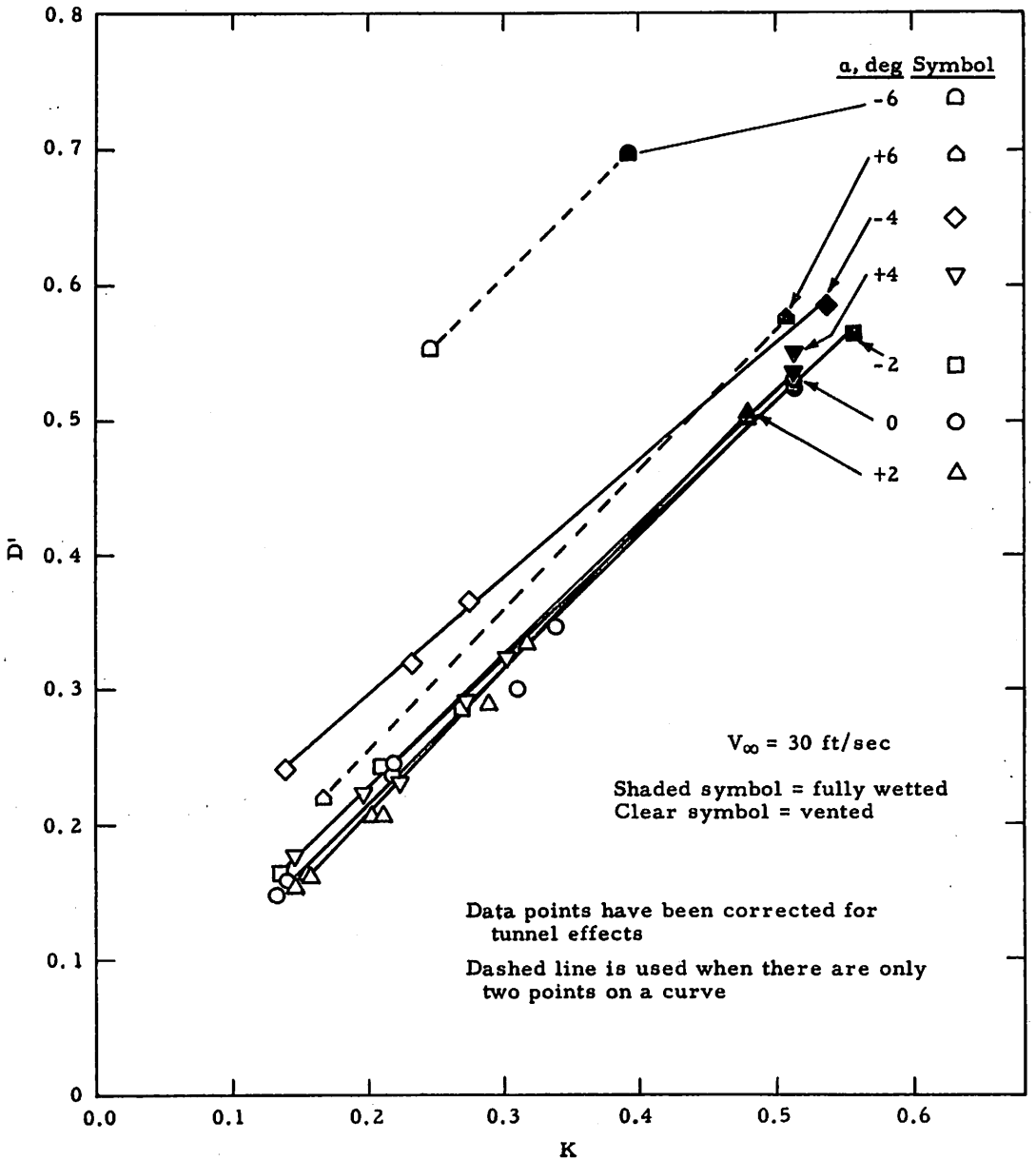

FIG. 23. D' Versus K for Various α Values With AR = ∞.

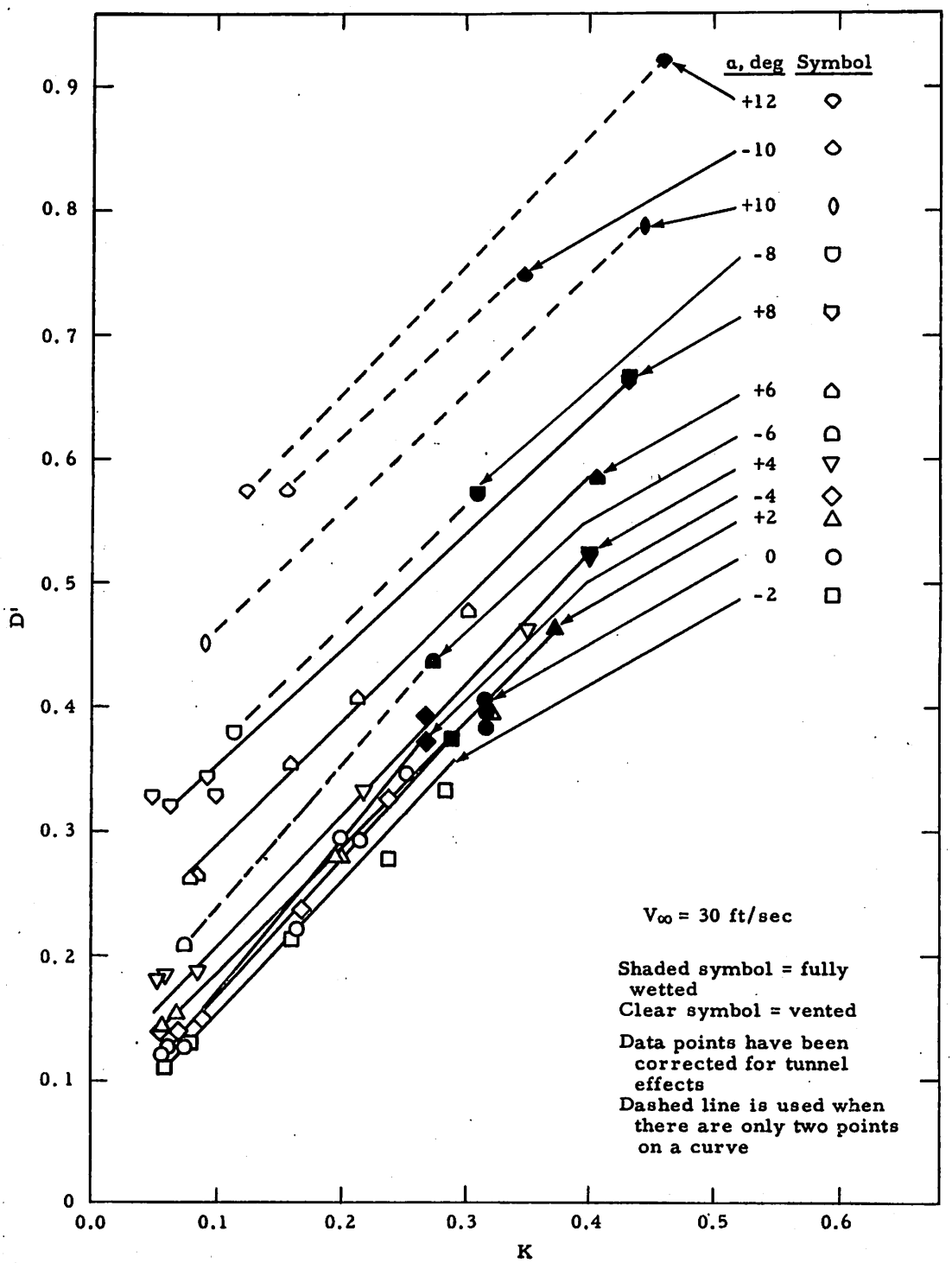

FIG. 24. D' Versus K for Various α Values With ÆR = 1.44.

and $\Delta D' = 0.056$ (average) for the closed-cavity curve. These values of $\Delta D'$ lie between the theoretical laminar friction drag, $D_f' = 0.016$ ($C_{Df} = 0.0024$), and the theoretical turbulent friction drag, $D_f' = 0.060$ ($C_{Df} = 0.0090$). Therefore it may be concluded that the experimental results are in good agreement with theory.

The most interesting and useful operating condition of a base-vented hydrofoil is the region around $K = 0$ where the cavity drag is lowest. Unfortunately the experimental results show that tunnel-blockage effects restrict the test range of K to $K > 0.14$ for $AR = \infty$ and $K > 0.06$ for $AR = 1.44$. These minimum values of K are in agreement with the tunnel-blockage theory discussed in Appendix B.

Figure 26 shows D' versus K for $\alpha = 0^\circ$ with $AR = 1.44$. In this case one side-wall was removed to provide a finite model span; this reduced the tunnel blockage and the ventilation number could be decreased to 0.06. When K is in this region, the slope of the curve D' versus K should theoretically begin to change, but it does not. For this reason, and to verify the critical airflow rate, it is planned to test models under different tunnel-blockage conditions to obtain data nearer $K = 0$. The corrections shown in Fig. 26 are for tunnel-interference effects and for induced drag and tip drag. The latter two corrections were made to permit comparison of the data with the two theoretical cavity-drag curves from Ref. 14. As in Fig. 25, the difference between the corrected experimental drag curve and the theoretical cavity drag curves is presumably the frictional drag. The difference between the experimental curve and the open-cavity drag curve is $\Delta D' = 0.045$ (average) and the difference between the experimental curve and the closed-cavity drag curve is $\Delta D' = 0.080$ (average). These values disagree somewhat with the frictional drag from Fig. 25, but still lie in the laminar and turbulent range. The disagreement may be due to errors in measurement, in the tunnel corrections, or in the boundary conditions of the linearized theory, in which tunnel-wall effects were not included.

LIFT-TO-DRAG RATIO

Perhaps the most important characteristic of lift-producing hydrofoils is their lift-to-drag ratio L/D, which is indicative of their efficiency. The experimental values of L/D for the case where $AR = \infty$ are plotted in Fig. 27 as a function of α. The maximum L/D ratio is 24 at $\alpha = 4.5^\circ$, when K had the minimum value of 0.14. If lower values of K could have been experimentally attained, higher values of L/D would have been measured. When the model was fully wetted, K was 0.50, and the maximum L/D was 11 at $\alpha = 8^\circ$.

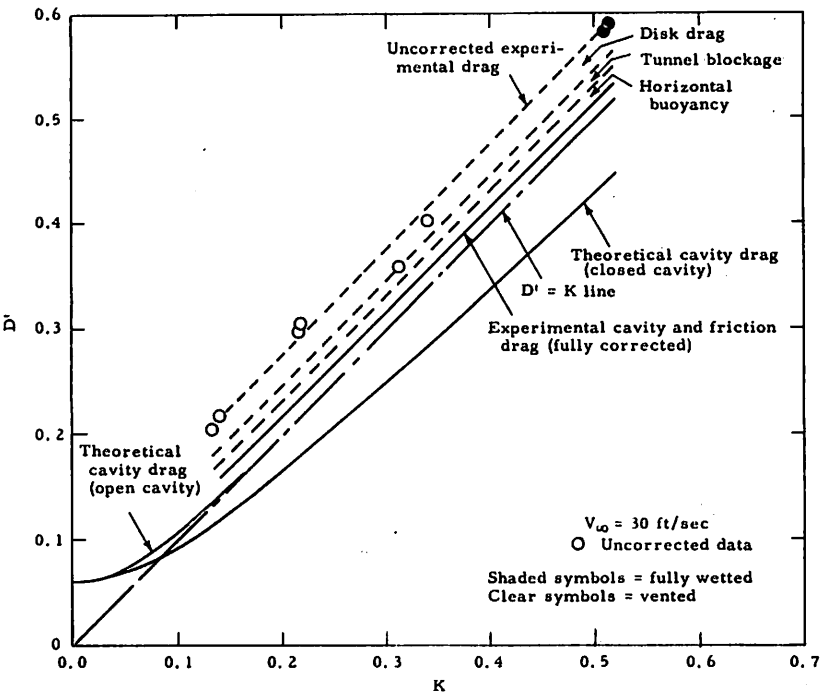

FIG. 25. D' Versus K for $\alpha = 0^\circ$ With $\mathcal{R} = \infty$, Including Tunnel Corrections and Theoretical Curve.

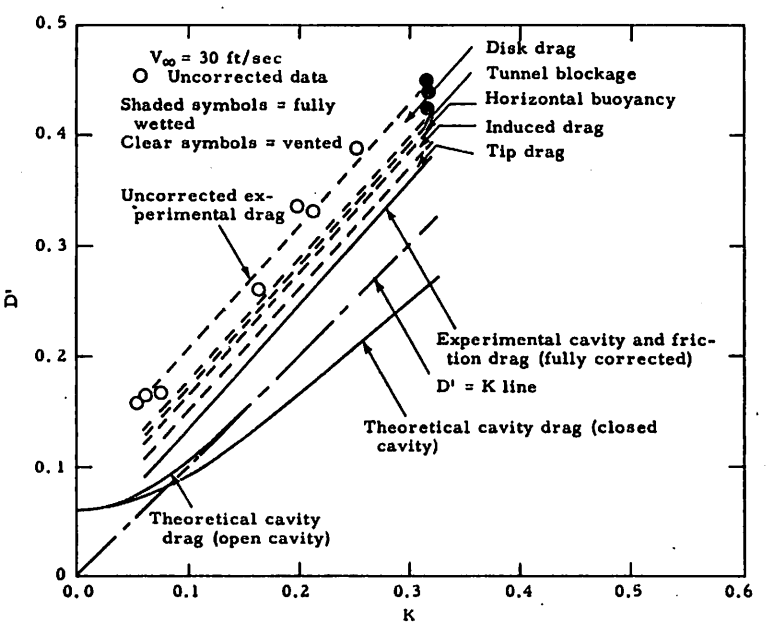

FIG. 26. D' Versus K for $\alpha = 0^\circ$ With $\mathcal{R} = 1.44$, Including Tunnel Corrections and Theoretical Curve.

The experimental values of L/D versus α when $\mathcal{AR}$ = 1.44 are plotted in Fig. 28. Due to the very low aspect ratio, the maximum L/D measured was 8.5 at $\alpha = 4^\circ$ when K was 0.06. When fully wetted, K was 0.36 and the maximum L/D was 4.0 in the range of α from 6 to 10°.

Theoretical estimates of the L/D ratio of different types of base-vented hydrofoils are made in Ref. 2. The L/D ratios of other types of base-vented hydrofoils are estimated to be higher than those of the cambered parabola, when no cavitation occurs. However, for hydrofoils traveling at high speed near the water surface (i.e., $\sigma < 0.28$ in one comparison) the base-vented cambered parabola is shown to have higher efficiency and structural strength than either the more conventional fully wetted streamlined hydrofoils or the supercavitating hydrofoils.

It is interesting to compare the experimental values of L/D with theoretical ones and to extrapolate the results to K = 0, in order to estimate the potential improvement. In Fig. 29 theoretical values of L/D are plotted as a function of α under the following assumptions:

1. The design lift coefficient $C_{L_d} = 0.40$ and $\alpha_d = 0^\circ$ when $\mathcal{AR} = \infty$

2. The lift coefficient derivative is

$$C'_{L_\alpha} = \frac{2\pi \mathcal{AR}}{\sqrt{\mathcal{AR}^2 + 4} + 2}$$

3. The design lift coefficient for $\mathcal{AR} \neq \infty$ is

$$C'_{L_d} = C_{L_d}\left(\frac{C'_{L_\alpha}}{2\pi}\right)$$

4. The induced drag is $C_{d_i} = C_L^2/\pi\mathcal{AR}$

5. The cavity drag is that predicted by the linearized closed-cavity theory

6. The separation drag is that obtained experimentally in this study (Fig. 22)

7. The tip drag is $C_{D_t} = 0.104\,(t/c)^2$

8. The frictional drag $C_{D_f} = 0.0090$.

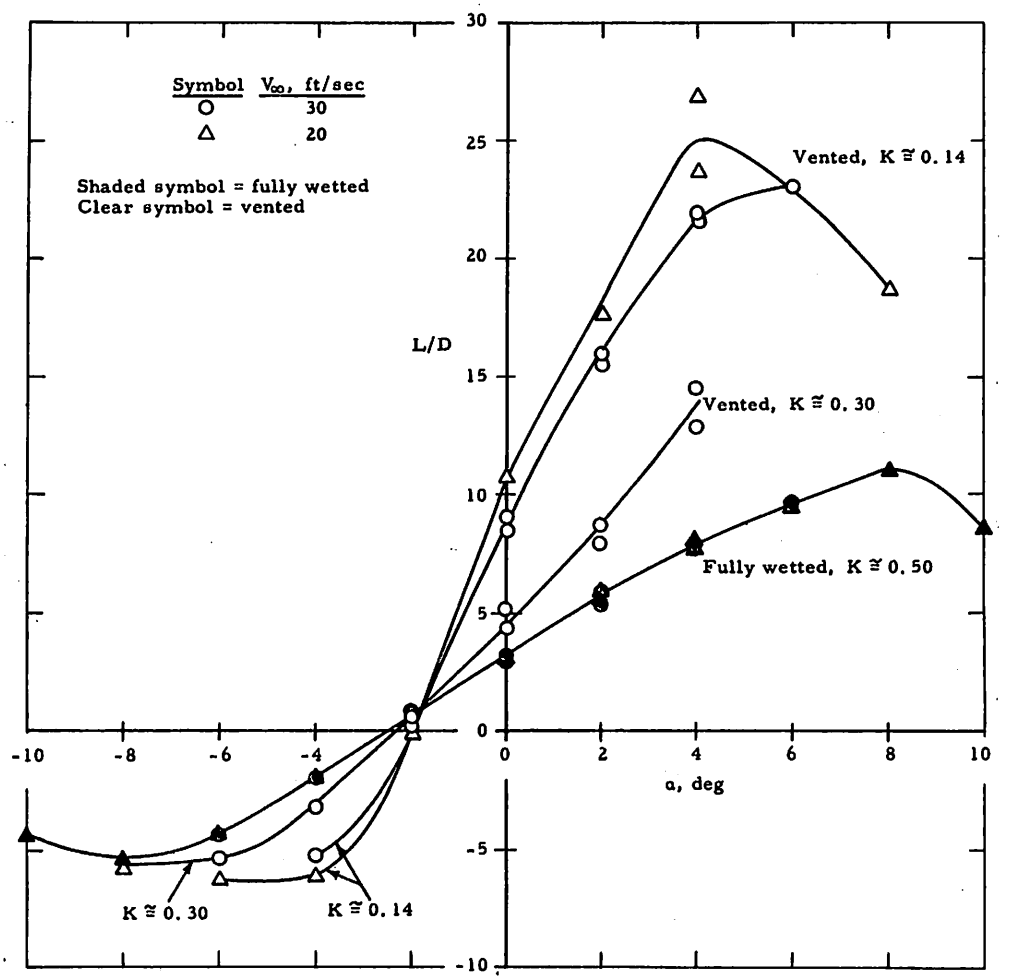

FIG. 27. .Experimental L/D Versus α With AR = ∞.

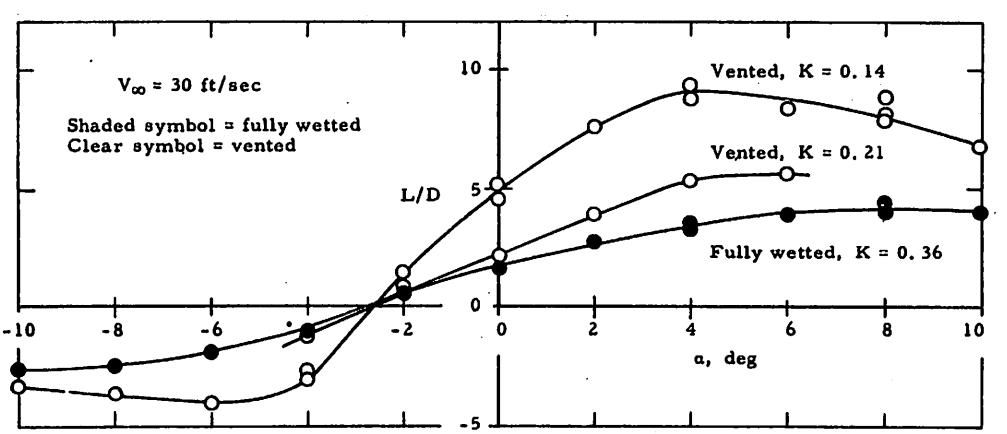

FIG. 28. Experimental L/D Versus α With AR = 1.44.

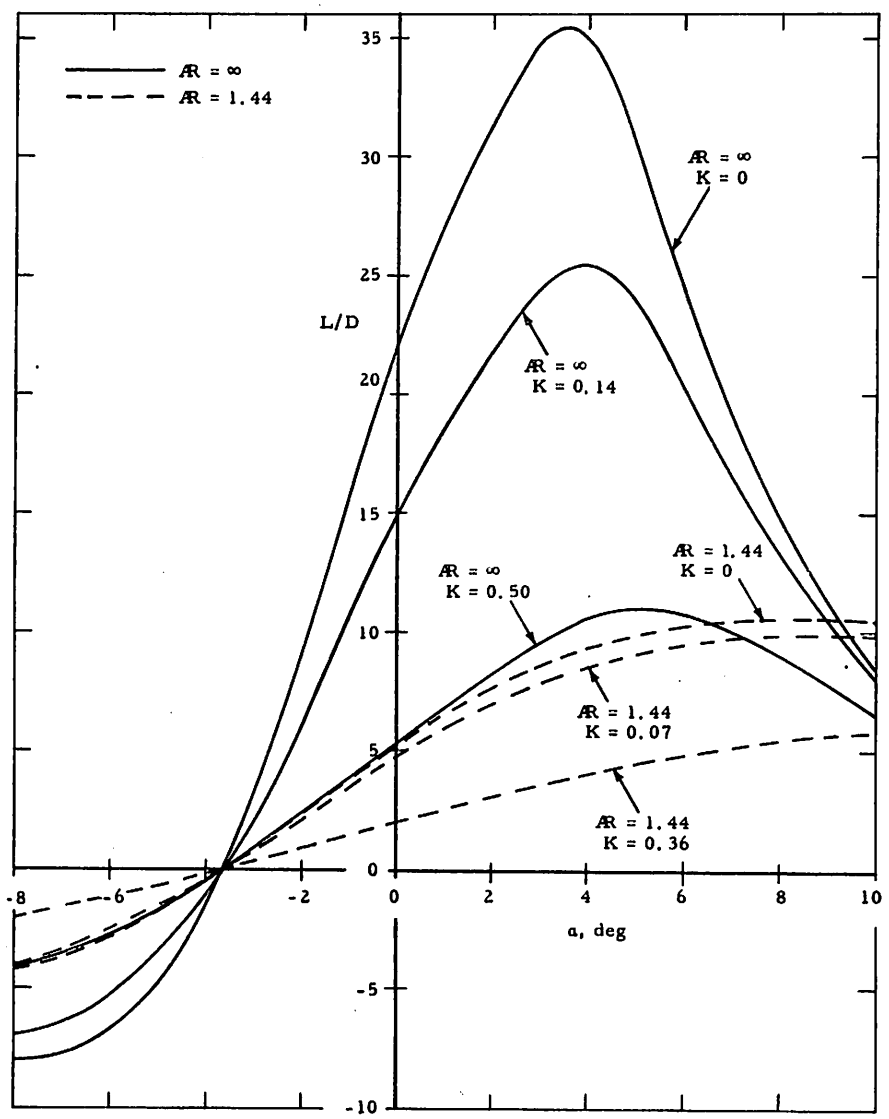

FIG. 29. Theoretical L/D Versus α With ÆR = ∞ and ÆR = 1.44.

The results of Fig. 29 show that, when K = 0, the maximum theoretical L/D for ÆR = ∞ is 35.5 at $\alpha = 3.5^{\circ}$. When K = 0.14, the maximum L/D is 25.5 at $\alpha = 4^{\circ}$, and when K = 0.50 it is 10.9 at $\alpha = 5^{\circ}$. The experimental maximum values of L/D were 24 at $\alpha = 5^{\circ}$ for K = 0.14 and 11 at $\alpha = 8^{\circ}$ for K = 0.50. Thus the experimental and theoretical values are in close agreement. The differences may be attributed to the fact that the design lift coefficient was not obtained in the experimental tests because of deviations in pressure from the pressure distribution of the NACA a = 1.0 camber line. Also plotted in Fig. 29 are the theoretical values of L/D for ÆR = 1.44, showing that when K = 0 the maximum L/D = 10.6 at $\alpha = 8.5^{\circ}$, when K = 0.07 L/D = 9.9 at $\alpha = 9^{\circ}$, and when K = 0.36 L/D $\cong$ 6 at $\alpha = 10^{\circ}$. These results are in fair agreement with the experimental results of L/D = 8.5 at $\alpha = 4^{\circ}$ for K = 0.07 and L/D = 4.0 at $\alpha = 6^{\circ}$ to 10° for K = 0.36.

INCIPIENT CAVITATION NUMBER

The incipient cavitation number σ_i of a hydrofoil is defined as the value of the free-stream cavitation number at which the hydrofoil begins to cavitate. σ_i is approximately equal to the negative value of the minimum pressure coefficient:

$$\sigma_i \cong -C_{p_{min}} = \frac{P_\infty - P_{min}}{q_\infty}$$

and by Bernoulli's equation ($P_\infty + q_\infty = P_{min} + q_{max}$):

$$\sigma_i \cong \frac{q_{max} - q_\infty}{q_\infty} = \left(\frac{V_{max}}{V_\infty} \right)^2 - 1$$

where V_{max} is the maximum flow velocity at some point on the surface of the hydrofoil.

According to Ref. 15, the flow velocity on the surface of an uncambered hydrofoil having a parabolic cross section, at zero angle of attack, is

$$V_t = V_\infty \sqrt{\frac{x'}{x' + r'/2}}$$

where r' and x' are the ratios to chord-length of the leading-edge radius and distance from the leading edge, respectively. For an accurately shaped parabolic cross section $r' = \tau^2/8$ where τ is the ratio of base thickness to chord.

The added velocity V_a caused by a small deviation $\alpha - \alpha_d$ of the angle of attack from the design angle α_d is

$$V_a = \pm V_\infty \frac{\alpha - \alpha_d}{\sqrt{x' + r'/2}}$$

where α and α_d are measured in radians and (+) and (-) refer to the upper and lower surfaces, respectively (Ref. 16).

If the parabola is cambered using the NACA a = 1.0 camber line, a further velocity increment V_c is added (Ref. 6).

$$V_c = \pm\left(\frac{C_{L_d}}{4}\right)V_\infty$$

where (+) and (-) refer to the upper and lower surfaces, respectively.

Summing the velocities, $V = V_t + V_a + V_c$, the incipient cavitation number of a cambered parabola at an angle of attack α is

$$\sigma_i = \left(\frac{V}{V_\infty}\right)^2_{max} - 1 = \left[\sqrt{\frac{x'}{x' + r'/2}} \pm \frac{(\alpha - \alpha_d)}{\sqrt{x' + r'/2}} \pm \frac{C_{L_d}}{4}\right]^2_{max} - 1$$

Upon setting $d/dx\,(V/V_\infty) = 0$, the chordwise location of the maximum velocity is found to be

$$x'_{max} = \frac{r'^2}{4(\alpha - \alpha_d)^2} \quad \text{or } x' = 1$$

Substituting,

$$\sigma_i \cong \frac{2(\alpha - \alpha_d)^2}{r'} \pm \frac{C_{L_d}}{2}\sqrt{\frac{2(\alpha - \alpha_d)^2}{r'} + 1}$$

(+) $\alpha > 0$, upper surface
(-) $\alpha < 0$, lower surface

or $\sigma_i \cong +2(\alpha - \alpha_d) + C_{L_d}/2$ (for x' = 1.0, upper surface) whichever is larger.

The experimental data points of incipient cavitation number σ_i are plotted in Fig. 30 as a function of angle of attack for $\mathcal{AR} = \infty$.

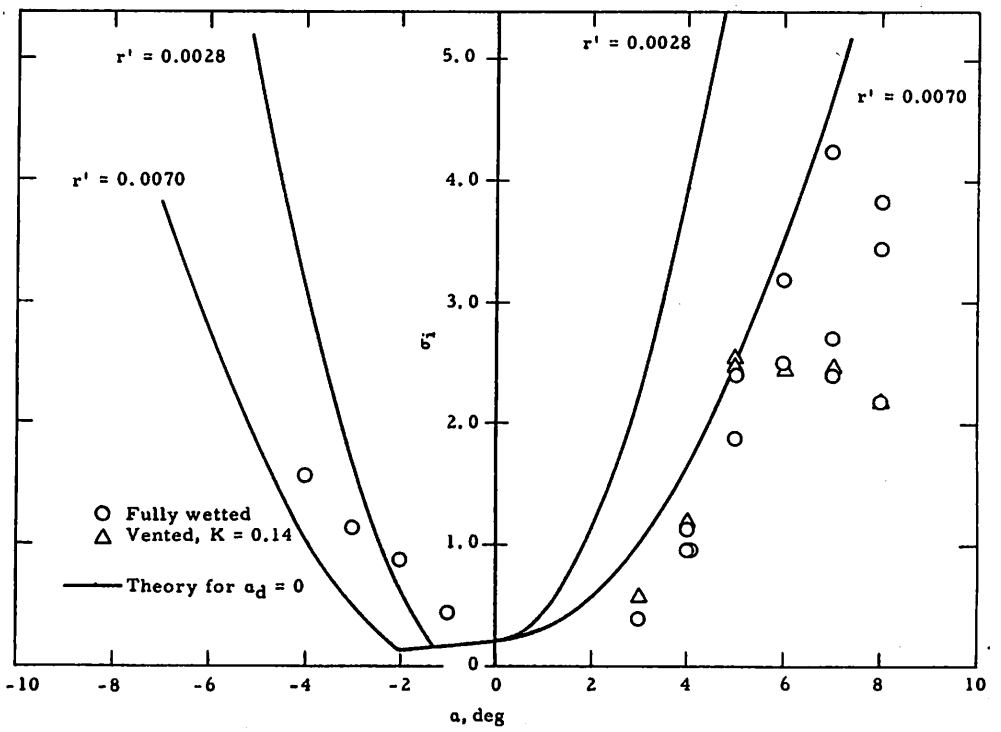

FIG. 30. σ_i Versus α With $\mathcal{AR} = \infty$, Experiment and Theory.

The theoretical values of σ_i are plotted as lines in Fig. 30, showing the incipient cavitation numbers of cambered parabolas whose leading edge radii are 0.0028c and 0.0070c. The design angle of attack α_d, was equated to zero in this graph, as it theoretically should be for the a = 1.0 camber line. In reality, due to the pressure deviation from theory, the design angle is probably between 0 and 1°; hence the theoretical curve of σ_i versus α should be shifted to the right. The theoretical leading-edge radius of an accurately formed parabola having a base-thickness-to-chord ratio $\tau = 0.15$ is 0.0028c. The measured leading-edge radius of the model varied along the span from 0.0030c to 0.0070c; a radius of 0.0070c would correspond to $\tau = 0.24$. In general, fair agreement is found between experiment and theory.

CONCLUSIONS

1. Results of water-tunnel tests on a base-vented hydrofoil, having a cambered parabolic cross section, show that the experimental values of lift, drag, moment, and incipient cavitation number are in agreement with experimental results for streamlined cross sections having the same camber line. The discrepancies between these and the theoretical values can be attributed to pressure deviations on the upper and lower surfaces that are believed to be caused by failure to attain the theoretical pressure discontinuities of the NACA a = 1.0 (uniform load) camber line.

2. The air cavity produced behind the base did not spring forward to the leading edge unless the hydrofoil stalled or extensive vapor cavitation occurred behind the leading edge. When K was less than 0.20, a thin, wispy type of ventilation occasionally appeared for about 1/8 chord-length on the upper surface ahead of the base, producing a small change in lift. This ventilation was believed to have been caused by local boundary-layer separation that occurred whenever the pressure gradient was unfavorable in this region.

3. A maximum lift/drag ratio of 24 was measured with $\mathcal{AR} = \infty$ at $\alpha = 4.5^{\circ}$, when the ventilation number of the cavity was K = 0.14. Higher lift/drag ratios would have been obtained if K could have been lowered, but this was prevented by tunnel-blockage effects. A maximum lift/drag ratio of 8.5 was measured with $\mathcal{AR} = 1.44$. In the latter case it was possible to reduce K to 0.06 because of decreased tunnel blockage. It is planned to conduct tests in the future under different conditions of tunnel blockage to obtain data nearer to K = 0.

4. The results of these tests tend to verify the potentially high efficiency and cavitation resistance of base-vented hydrofoils pointed out in Ref. 2.

Appendix A

COORDINATES OF HYDROFOIL CROSS SECTION

Parabolic Thickness Distribution, 15% Thickness Ratio
C_{L_d} = 0.40, NACA a = 1.0 Camber Line

x/c	y/c (Upper)	y/c (Lower)
0.0000	0.0000	0.0000
0.0050	0.0063	0.0043
0.0075	0.0079	0.0051
0.0125	0.0105	0.0062
0.025	0.0156	0.0081
0.050	0.0231	0.0105
0.075	0.0290	0.0121
0.10	0.0340	0.0134
0.15	0.0425	0.0156
0.20	0.0495	0.0176
0.25	0.0554	0.0196
0.30	0.0605	0.0216
0.35	0.0649	0.0237
0.40	0.0689	0.0260
0.45	0.0722	0.0284
0.50	0.0751	0.0309
0.55	0.0775	0.0337
0.60	0.0795	0.0366
0.65	0.0811	0.0399
0.70	0.0822	0.0433
0.75	0.0828	0.0470
0.80	0.0830	0.0512
0.85	0.0826	0.0557
0.90	0.0815	0.0609
0.95	0.0794	0.0668
1.00	0.0750	0.0750

Appendix B

CORRECTIONS FOR TUNNEL-INTERFERENCE EFFECTS

The flow pattern around a hydrofoil model in an enclosed water tunnel differs from that around a hydrofoil in a free fluid. The effects of boundary constraint are complex. The interference is usually divided into several components whose effects are assumed to be additive: solid blockage, wake blockage, lift effect, and horizontal static-pressure gradient (horizontal buoyancy). The equations for these corrections were obtained from Pankhurst and Holder (Ref. 8); the effect of the boundary layer on the tunnel walls upon the lift of the hydrofoil has been found to be negligible.

The corrections given in Ref. 8 apply to fully wetted models only. There are no equations available as yet for estimating the tunnel-interference effects in cavitating flow. In the present case, however, the fully wetted and base-vented flow patterns are similar, since in fully wetted flow there is a wake behind the blunt base which closely resembles the shape of the cavity. Therefore the correction formulas were assumed to be equally valid for both fully wetted and base-vented flow.

The infinite-aspect-ratio tests were made in a nearly rectangular, closed working section, formed by placing two parallel vertical plates into the original circular working section of the water tunnel. For the finite-aspect-ratio tests, one of these side plates was removed, making the tunnel cross section a circular segment.

The corrections given here are in the form:

$$\Delta(\ ) = (\ )_{\text{free stream}} - (\ )_{\text{measured}}$$

The coefficients used in the equations are the measured values.

BLOCKAGE AND LIFT EFFECTS

The solid and wake blockage corrections are for the increase in axial velocity past the hydrofoil and its wake, due to the partial blocking of the flow. The lift effect is due to the constraint of the

tunnel walls on the curved streamlines, which effectively changes the hydrofoil camber and angle of attack.

Infinite Aspect Ratio

The important parameters of the rectangular working section, and of the model, are

h = height of working section = 14 in.
c = model chord length = 4 in.
b = span of working section and model = 3 in.
t = maximum (base) thickness of model = 0.6 in.

The correction for solid and wake blockage is

$$\frac{\Delta C_L}{C_L} = \frac{\Delta C_D}{C_D} \cong -2\left[0.41\left(1+\frac{c}{t}\right)\left(\frac{t}{h}\right)^2 + \frac{1}{4}\frac{c}{h} C_D\right] = -2\% \text{ to } -3\%$$

The corrections for the lift effect are

$$\frac{\Delta C_L}{C_L} = -\frac{\pi^2}{24}\left(\frac{c}{h}\right)^2 \frac{(C_L + 2C_M)}{C_L}, \quad -0.0308 \leq \Delta C_L \leq +0.0273,$$

$$\Delta C_L \sim -0.0023 \text{ at } \alpha = 0^\circ$$

$$\frac{\Delta C_M}{C_M} = \frac{\pi^2}{192}\left(\frac{c}{h}\right)^2 \frac{C_L}{C_M} = -5\% \text{ to } +3\%$$

$$\frac{\Delta C_D}{C_D} = \frac{\pi}{96}\left(\frac{c}{h}\right)^2 \frac{(C_L + 4C_M)C_L}{C_D} = -0.2\% \text{ to } +1.2\%$$

(not applied to data)

Finite Aspect Ratio

The corrections for the circular-segment working section have been estimated using an equivalent rectangular working section of span b = 3 inches and height h_e such that the areas of the circular segment and equivalent rectangle are equal:

Let

$$bh_e = \text{area of circular segment} = 97.8 \text{ in}^2$$

$$h_e = \frac{97.8}{3} = 32.62 \text{ in.}$$

It is then assumed that the infinite aspect ratio correction formulas apply, if h is replaced by h_e.

The magnitudes of the finite aspect ratio corrections are

Solid and wake blockage

$$\frac{\Delta C_L}{C_L} = \frac{\Delta C_D}{C_D} = 0.3\% \text{ to } 1.1\%$$

Lift effect

$$-0.0030 \leq \Delta C_L \leq +0.0024 \text{ (not applied to data)}$$

$$\frac{\Delta C_D}{C_D} = -0.03\% \text{ to } +0.07\% \text{ (not applied to data)}$$

$$\frac{\Delta C_M}{C_M} = -0.9\% \text{ to } +0.4\% \text{ (not applied to data)}$$

HORIZONTAL BUOYANCY EFFECTS

The horizontal static-pressure gradient (horizontal buoyancy) is caused by the thickening of the boundary layer on the tunnel walls; the model is thus being tested in a tunnel whose walls seem to be converging. The gradient could be eliminated if the tunnel walls were designed to diverge an amount equal to the thickening of their boundary layers.

Infinite Aspect Ratio

The horizontal static-pressure gradient in the empty rectangular working section is (from Ref. 5)

$$\frac{d}{dx}\left(\frac{P_\infty}{q_\infty}\right) = -0.056 \text{ ft}^{-1}$$

The midchord point of the model was 5 inches downstream of the static-pressure tap.

The drag correction due to horizontal buoyancy is

$$\Delta C_D = (1 + 1.2\tau)\frac{A_x}{c}\frac{d}{dx}\left(\frac{P_\infty}{q_\infty}\right) = -0.0022$$

$$\frac{\Delta C_D}{C_D} \cong -1\% \text{ to } -7\%$$

where

τ = base-thickness-to-chord ratio = 0.15
A_x = chordwise cross-sectional area of model = 1.61 in^2

The lift and moment are not affected.

The effects of horizontal buoyancy are more complex for vented models than for fully wetted models. The influence of the "converging tunnel walls" on the cavity pressure and drag has not been investigated. Therefore, the above drag correction has been used for the vented cases, also.

The measured cavity pressure, and hence the measured ventilation number K, is based upon the static pressure 5 inches upstream of the model midchord. K has been corrected to the local static pressure at the leading edge of the cavity, 7 inches downstream of the pressure tap, as follows:

$$\Delta K = \Delta\left(\frac{P_\infty - P_c}{q_\infty}\right) = \frac{\Delta P_\infty}{q_\infty} = \frac{7}{12}(-0.056) = -0.0326$$

$$\frac{\Delta K}{K_{min}} = -19.2\%$$

This correction is open to question, since the exact location at which the static pressure should be measured to determine K is unknown.

Finite Aspect Ratio

The horizontal static-pressure gradient in the circular-segment working section can be estimated. The first step is to calculate the rate of increase, with distance, of the displacement thickness of the boundary layer on the walls of the rectangular working section, in terms of the tunnel dimensions and measured static-pressure gradient.

The following nomenclature is used:

A = effective area of cross section of tunnel (exclusive of boundary layer)

p = perimeter of cross section of tunnel

P = tunnel static pressure

q = tunnel dynamic pressure

V = tunnel velocity

The following subscripts indicate where the above values are measured:

o = at static-pressure tap in rectangular section

1 = at axis of spindle in rectangular section

2 = at static-pressure tap in circular-segment section

3 = at axis of spindle in circular-segment section

and

$B_o = \frac{d}{dx}\left(\frac{P_\infty}{q_\infty}\right)_o$ = horizontal static-pressure gradient in rectangular working section

$B_2 = \frac{d}{dx}\left(\frac{P_\infty}{q_\infty}\right)_2$ = horizontal static-pressure gradient in circular-segment working section

θ = displacement thickness of the boundary layer

$\left(\frac{d\theta}{dx}\right)_o$ = rate of change of θ on walls of rectangular working section

$\left(\frac{d\theta}{dx}\right)_2$ = rate of change of θ on walls of circular-segment working section

x_t = distance along tunnel center line from pressure tap to spindle axis

By the equation of continuity,

$$A_o V_o = A_1 V_1$$

hence

$$\frac{A_o^2}{A_1^2} = \frac{V_1^2}{V_o^2} = \frac{q_1}{q_o}$$

By Bernoulli's equation,

$$P_o + q_o = P_1 + q_1$$

Using these relations,

$$B_o x_t = \frac{d}{dx}\left(\frac{P_\infty}{q_\infty}\right) \cdot x_t \cong \frac{P_1 - P_o}{q_o} = \frac{q_o - q_1}{q_o} = 1 - \frac{q_1}{q_o} = 1 - \frac{A_o^2}{A_1^2}$$

hence

$$\frac{A_o}{A_1} = \sqrt{1 - B_o x_t} \cong 1 - \frac{1}{2} B_o x_t$$

Considering the growth of the boundary layer,

$$A_1 \cong A_o - x_t p_1 \left(\frac{d\theta}{dx}\right)_o$$

hence

$$\frac{A_o}{A_1} = \frac{A_o}{A_o - x_t p_1 \left(\frac{d\theta}{dx}\right)_o} = \frac{1}{1 - \frac{x_t p_1}{A_o}\left(\frac{d\theta}{dx}\right)_o} \cong 1 + \frac{x_t p_1}{A_o}\left(\frac{d\theta}{dx}\right)_o$$

therefore

$$1 - \frac{1}{2} B_o x_t \cong 1 + \frac{x_t p_1}{A_o} \left(\frac{d\theta}{dx} \right)_o$$

or

$$\left(\frac{d\theta}{dx} \right)_o \cong - \frac{1}{2} B_o \frac{A_o}{p_1}$$

This expression may now be used in determining the approximate horizontal pressure gradient in the circular-segment working section.

By the same reasoning as above,

$$\left(\frac{d\theta}{dx} \right)_2 \cong - \frac{1}{2} B_2 \frac{A_2}{p_3}$$

It is now assumed that

$$\left(\frac{d\theta}{dx} \right)_2 = \left(\frac{d\theta}{dx} \right)_o$$

Then

$$B_2 = \frac{A_o}{A_2} \frac{p_3}{p_1} B_o$$

Since

$$p_1 = 34 \text{ in.}$$

$$p_3 = 39 \text{ in.}$$

$$A_o = 42 \text{ in}^2$$

$$A_2 = 97.8 \text{ in}^2$$

we have

$$B_2 = 0.493 \, B_o = (0.493)(-0.056) = -0.028 \text{ ft}^{-1}$$

Using this value for horizontal static-pressure gradient, and the correction equations given for infinite aspect ratio,

$$\Delta C_D = -0.0011$$

$$\frac{\Delta C_D}{C_D} = -1\% \text{ to } -6\%$$

$$\Delta K = -0.016$$

$$\frac{\Delta K}{K_{min}} = -22.5\%$$

MINIMUM VENTILATION NUMBER

For a given tunnel and model, there is a minimum ventilation number K_{min} which is reached when the cavity extends infinitely far downstream. In this case the tunnel is said to be "choked." Further increases in air-flow rate will not decrease K below K_{min}. If horizontal buoyancy effects are neglected, the value of K_{min} may be estimated using the following equation from Ref. 17:

$$C_D \text{ (at } K_{min}) = \frac{A_o}{A}\left[\sqrt{1 + K_{min}} - 1\right]^2$$

Using theoretical values of C_D versus K from Fig. 24, it is found that

$$K_{min} \cong 0.16 \text{ for infinite aspect ratio}$$

$$K_{min} \cong 0.08 \text{ for finite aspect ratio}$$

The experimental values of K_{min} were 0.13 and 0.06 for infinite and finite aspect ratios, respectively.

CORRECTIONS TO INCIPIENT CAVITATION NUMBER

The measured incipient cavitation number was based upon static and dynamic pressures measured 3 inches upstream of the model's leading edge. The free-stream incipient cavitation number will be determined by the local tunnel conditions at the leading edge. The pressures at the leading edge are affected by solid and wake blockage and by horizontal buoyancy. The method of correcting σ_i is as follows:

Let

$$\sigma_{i_m} = \frac{P_m - P_v}{q_m} \cong \frac{P_m}{q_m} \text{ (measured)}$$

$$\sigma_i = \frac{P_\infty - P_v}{q_\infty} \cong \frac{P_\infty}{q_\infty} \text{ (corrected)}$$

where P_m, q_m are values 3 inches upstream of the model and P_∞, q_∞ are values at the model leading edge.

Bernoulli's equation states

$$P_\infty + q_\infty = P_m + q_m$$

Hence

$$\sigma_i \cong \frac{P_\infty}{q_\infty} = \frac{P_m}{q_\infty} + \frac{q_m}{q_\infty} - 1 = \frac{P_m}{q_m}\left(\frac{q_m}{q_\infty}\right) + \frac{q_m}{q_\infty} - 1$$

or

$$\sigma_i \cong \sigma_{i_m}\left(\frac{q_m}{q_\infty}\right) + \frac{q_m}{q_\infty} - 1$$

q_m/q_∞ is evaluated as follows: if we let

$$\Delta q = q_\infty - q_m$$

then

$$\frac{q_\infty}{q_m} = 1 + \frac{\Delta q}{q_m}$$

Now, with "h. b." indicating horizontal buoyancy and "block." indicating blockage,

$$\frac{\Delta q}{q_m} = \left(\frac{\Delta q}{q_m}\right)_{\text{h. b.}} + \left(\frac{\Delta q}{q_m}\right)_{\text{block.}}$$

where

$$\left(\frac{\Delta q}{q_m}\right)_{h.\,b.} = -\left(\frac{P_\infty - P_m}{q_m}\right)_{h.\,b.} = -(-0.056)\frac{3\text{ in.}}{12\text{ in.}} = 0.014$$

and

$$\left(\frac{\Delta q}{q_m}\right)_{block.} = \left(\frac{q_\infty}{q_m}\right)\left(\frac{\Delta q}{q_\infty}\right)_{block.} = \left(1 + \frac{\Delta q}{q_m}\right)\left(\frac{\Delta q}{q_\infty}\right)_{block.}$$

$$= \left(\frac{\Delta q}{q_\infty}\right)_{block.} \cdot \left[1 + \left(\frac{\Delta q}{q_m}\right)_{h.\,b.} + \left(\frac{\Delta q}{q_m}\right)_{block.}\right]$$

$$\left(\frac{\Delta q}{q_m}\right)_{block.} = \frac{(\Delta q/q_\infty)_{block.}\left[1 + (\Delta q/q_m)_{h.\,b.}\right]}{1 - (\Delta q/q_\infty)_{block.}}$$

but

$$\left(\frac{\Delta q}{q_\infty}\right)_{block.} = -\left(\frac{\Delta C_L}{C_L}\right)_{block.} \cong 0.0234 \quad (a = 0^\circ)$$

so

$$\left(\frac{\Delta q}{q_m}\right)_{block.} = 0.0243$$

and

$$\frac{q_\infty}{q_m} = 1 + \left(\frac{\Delta q}{q_m}\right)_{h.\,b.} + \left(\frac{\Delta q}{q_m}\right)_{block.} = 1 + 0.014 + 0.0243 = 1.038$$

Finally,

$$\frac{q_m}{q_\infty} = \frac{1}{1.038} = 0.963$$

and

$$\sigma_i = \sigma_{i_m} (0.963) + 0.963 - 1$$

or

$$\sigma_i = 0.963\ \sigma_{i_m} - 0.037$$

Appendix C

AIR-FLOW DATA REDUCTION

The air flowmeter is calibrated to measure the air-flow rate at standard room temperature and standard pressure P_s. Since the air passing through the meter is at the supply-line pressure P_ℓ, the meter reading Q_m must be corrected. The meter reading Q_m is proportional to the air-flow velocity entering the meter and the square root of the air density. Since the supply-line air is at room temperature, its density will be proportional to its pressure P_ℓ, hence:

$$Q_m = Q_\ell \sqrt{\frac{P_\ell}{P_s}} \quad \text{or} \quad Q_\ell = Q_m \sqrt{\frac{P_s}{P_\ell}}$$

The air-flow rate Q based on the free-stream static pressure P_∞ is $Q = Q_\ell(P_\ell/P_\infty)$. It is assumed that the air lines from the flowmeter to the working section are sufficiently long that the flow is isothermal. Hence, the air-flow rate at a pressure P_∞ is

$$Q = Q_\ell \frac{P_\ell}{P_\infty} = Q_m \frac{P_\ell}{P_\infty} \sqrt{\frac{P_s}{P_\ell}}$$

The dimensionless air-flow rate is defined as:

$$Q' = \frac{Q}{V_\infty A_b}$$

The actual cavity pressure P_c is slightly different from the free-stream static pressure P_∞, but since the difference is small, the actual air-flow rate is approximately equal to Q.

REFERENCES

1. David Taylor Model Basin. Linearized Theory for Flows About Lifting Foils at Zero Cavitation Number, by M. P. Tulin and M. P. Burkart. Washington, DTMB, February 1955. (DTMB Report C-638.)
2. U. S. Naval Ordnance Test Station. Base-Vented Hydrofoils, by T. G. Lang. China Lake, Calif., NOTS, 19 October 1959. (NAVORD Report 6606, NOTS TP 2346.)
3. ———. Water-Tunnel Tests of Hydrofoils With Forced Ventilation, by Thomas G. Lang, Dorothy A. Daybell, and Kenneth E. Smith. China Lake, Calif., NOTS, 10 November 1959. (NAVORD Report 7008, NOTS TP 2363.)
4. Knapp, R. T., J. Levy, J. P. O'Neill, F. B. Brown. "The Hydrodynamics Laboratory of the California Institute of Technology," AM SOC MECH ENG, TRANS, Vol. 70, No. 5 (July 1948), pp. 437 - 57.
5. California Institute of Technology. Water Tunnel Tests of NACA 4412 and Walchner Profile 7 Hydrofoils in Noncavitating and Cavitating Flows, by R. W. Kermeen. Pasadena, Calif., CIT, February 1956. (CIT Hydrodynamics Laboratory Report No. 47-5.)
6. National Advisory Committee for Aeronautics. Summary of Airfoil Data, by I. H. Abbott, A. E. von Doenhoff, and L. S. Stivers. Washington, NACA, 1945. (NACA Report No. 824.)
7. California Institute of Technology. The High Speed Water Tunnel Three Component Force Balance, by G. M. Hotz and J. T. McGraw. Pasadena, Calif., CIT, January 1955. (CIT Hydrodynamics Laboratory Report No. 47-1.)
8. Pankhurst, R. D., and D. W. Holder. Wind Tunnel Technique. London, Pitman and Sons, 1952. Chapter 8.
9. National Advisory Committee for Aeronautics. A Simple Method for Estimating the Subsonic Lift and Damping in Roll of Sweptback Wings, by E. C. Polhamus. Washington, NACA, 1949. (NACA Technical Memorandum 1862.)
10. Hoerner, S. F. Fluid-Dynamic Drag. Midland Park, N. J., 1958. (Published by author.)

11. National Aeronautics and Space Administration. Investigation of a High-Speed Hydrofoil with Parabolic Thickness Distribution, by Virgil E. Johnson, Jr., and Thomas A. Rasnick. Washington, NASA, November 1959. (NASA TN D-119.)

12. California Institute of Technology. A Simple Method for Calculating the Drag in the Linear Theory of Cavity Flows, by T. Yao-tsu Wu. Pasadena, Calif., CIT, August 1957. (CIT Engineering Division Report No. 85-5.)

13. David Taylor Model Basin. Steady Two-Dimensional Cavity Flows About Slender Bodies, by M. P. Tulin. Washington, DTMB, May 1953. (DTMB Report 834.)

14. U. S. Naval Ordnance Test Station. Application of Thin-Airfoil Theory to Hydrofoils With Cut-off, Ventilated Trailing Edge, by Andrew G. Fabula. China Lake, Calif., NOTS, 13 September 1960. (NAVWEPS Report 7571, NOTS TP 2547.)

15. National Advisory Committee for Aeronautics. Subsonic Edges in Thin-Wing and Slender-Body Theory, by Milton D. Van Dyke. Washington, NACA, November 1954. (NACA TN 3343.)

16. Douglas Aircraft Co., Inc. Pressure Distribution at the Nose of a Thin Lifting Airfoil, by Anatol Roshko. Santa Monica, Calif., Douglas, November 1958. (Report No. SM 23368.)

17. Birkoff, G., M. Plesset, and N. Simmons. "Wall Effects in Cavity Flow." Part I, QUART APPL MATH, Vol. 8, No. 2 (July 1950), Part II, QUART APPL MATH, Vol. 9, No. 4 (January 1952).

INITIAL DISTRIBUTION

9 Chief, Bureau of Naval Weapons
- DIS-31 (1)
- R-12 (1)
- RAAD-3 (1)
- RRRE (1)
- RRRE-71 (1)
- RRSY (1)
- RU (1)
- RUAW (1)
- RUAW-42 (1)

6 Chief, Bureau of Ships
- Code 106 (1)
- Code 335 (1)
- Code 421 (2)
- Code 442 (1)
- Code 664 (1)

1 Chief, Bureau of Yards and Docks (Research Division)
1 Chief of Naval Operations
3 Chief of Naval Research
- Code 429 (1)
- Code 438 (1)
- Code 466 (1)

8 David W. Taylor Model Basin
- Code 142 (1)
- Code 500 (1)
- Code 513 (1)
- Code 523B (1)
- Code 526 (1)
- Code 580 (1)
- Code 800 (1)

1 Naval Academy, Annapolis (Librarian)
1 Naval Air Development Center, Johnsville
1 Naval Aircraft Torpedo Unit, Quonset Point
1 Naval Civil Engineering Laboratory, Port Hueneme (Code L54)
1 Naval Engineering Experiment Station, Annapolis
2 Naval Ordnance Laboratory, White Oak
- Library Division, Desk HL (1)

1 Naval Postgraduate School, Monterey (Library, Technical Reports Section)

1 Naval Research Laboratory
1 Naval Torpedo Station, Keyport (Quality Evaluation Laboratory, Technical Library)
1 Naval Underwater Ordnance Station, Newport
1 Naval Weapons Laboratory, Dahlgren
2 Naval Weapons Plant (Code 752)
1 Navy Central Torpedo Office, Newport
1 Navy Electronics Laboratory, San Diego
1 Navy Mine Defense Laboratory, Panama City
1 Navy Underwater Sound Laboratory, Fort Trumbull
1 Office of Ordnance Research, Durham
1 Waterways Experiment Station, Vicksburg
1 Air Force Office of Scientific Research (Mechanics Division)
1 Air Research and Development Command, Andrews Air Force Base
10 Armed Services Technical Information Agency (TIPCR)
1 Director of Defense (R & E) (Office of Fuels, Materials and Ordnance, Byard Belyea)
1 Committee on Undersea Warfare
1 Langley Research Center (John Parkinson)
1 Maritime Administration (Coordinator for Research)
1 Merchant Marine Academy, Kings Point, N. Y. (Head, Department of Engineering)
6 National Aeronautics and Space Administration
1 National Bureau of Standards (Fluid Mechanics Section, Dr. G. Schubauer)
2 National Science Foundation
Director (1)
Director, Engineering Sciences Division (1)
1 Office of Technical Services
5 British Joint Services Mission (Navy Staff), via BuWeps (DSC)
2 Defence Research Member, Canadian Joint Staff (W), via BuWeps (DSC)
1 Aerojet-General Corporation, Azusa, Calif. (C. A. Gongwer), via BuWepsRep
1 Aeronutronic Systems, Inc., Newport Beach, Calif. (Ralph E. Smith)
1 Alden Hydraulic Laboratory, Worcester Polytechnic Institute, Worcester, Mass.
1 American Mathematical Society, Providence, R. I. (Editor, Mathematical Reviews)
1 Applied Physics Laboratory, University of Washington, Seattle
1 AVCO Research Laboratory, Everett, Mass. (Technical Librarian)
1 Baker Manufacturing Company, Evansville, Wisc.
1 Bell Aerosystems Company, Buffalo (Technical Library)
1 Bell Telephone Laboratories, Murray Hill, N. J.

1 Bendix Aviation Corporation, Pacific Division, North Hollywood
1 Boeing Airplane Company, Seattle (Aero-Space Division Library)
2 Brown University, Providence, R. I.
  Division of Applied Mathematics (1)
  Division of Engineering, Prof. D. Drucker (1)
1 Bulova Research and Development Laboratories, Inc., Woodside, N. Y.
4 California Institute of Technology, Pasadena (Engineering Division)
  Dr. A. J. Acosta (1)
  Dr. C. B. Millikan (1)
  Dr. M. S. Plesset (1)
  Dr. T. Y. Wu (1)
1 Case Institute of Technology, Cleveland (Department of Mechanical Engineering, Prof. G. Kuerti)
1 Chance Vought Aircraft, Inc., Dallas (Engineering Library)
1 Cleveland Pneumatics Industries, Inc., El Segundo, Calif. (Advanced Systems Development Division)
1 Clevite Research Center, Cleveland
2 Colorado State University, Fort Collins (Department of Civil Engineering)
  Prof. J. E. Cermak (1)
  Prof. M. Albertson (1)
1 CONVAIR Hydrodynamics Laboratory, San Diego
1 CONVAIR Scientific Research Laboratory, San Diego (A. L. Berlad)
1 Cornell University Graduate School of Aeronautical Engineering, Buffalo (Prof. W. R. Sears)
2 Davidson Laboratory, Stevens Institute of Technology, Hoboken, N. J.
  A. Suarez (1)
  Dr. J. Breslin (1)
1 Douglas Aircraft Company, Inc., El Segundo, Calif. (Aerodynamics Section, A. M. O. Smith)
1 Eastern Research Group, Brooklyn (Dr. L. Meyerhoff)
1 EDO Corporation, College Point, N. Y. (S. Fenn)
1 Electric Boat Division, General Dynamics Corporation, Groton, Conn.
1 Engineering Societies Library, New York
1 General Electric Company, Missile and Ordnance Systems Department, Pittsfield, Mass. (Engineering Librarian)
1 General Electric Company, Schenectady (Librarian, LMEE Department)
1 Gibbs and Cox, Inc., New York (Dr. S. Hoerner)
1 Grumman Aircraft Engineering Corporation, Bethpage, N. Y. (Chief of Preliminary Design)
1 Grumman Aircraft Engineering Corporation, Dynamics Development Division, Babylon, N. Y.

2 Harvard University, Cambridge, Mass.
  Department of Mathematics, Prof. G. Birkoff (1)
  Department of Engineering Sciences, Prof. G. F. Carrier (1)
1 Hudson Laboratories, Columbia University, Dobbs Ferry, N. Y.
1 Hughes Aircraft Company, Culver City, Calif.
2 Hydrodynamics Laboratory, CIT, Pasadena
  Dr. V. A. Vanoni (1)
  T. Kiceniuk (1)
1 Hydronautics, Inc., Rockville, Md.
1 Illinois Institute of Technology, Chicago (Head, Department of Mechanical Engineering)
1 Institute of the Aerospace Sciences, Inc., New York (Librarian)
1 Johns Hopkins University, Baltimore (Head, Department of Mechanical Engineering)
1 Lehigh University, Bethlehem, Pa. (Civil Engineering Department, Prof. J. B. Herbich)
1 Lockheed Aircraft Corporation, Burbank, Calif.
1 Lockheed Aircraft Corporation, Missiles and Space Division, Palo Alto, Calif. (R. W. Kermeen)
3 Massachusetts Institute of Technology, Cambridge
  Department of Naval Architecture and Marine Engineering
    Prof. L. Troost (1)
    Prof. M. Abkowitz (1)
  Department of Civil Engineering, Prof. A. Ippen (1)
1 McDonnell Aircraft Corporation, St. Louis
1 Miami Shipbuilding Corporation, Miami (P. Buhlar)
1 New York State Maritime College, Fort Schuyler (Engineering Department, Prof. J. J. Foody)
1 New York University, Institute of Mathematical Science, New York
1 North American Aviation, Inc., Los Angeles (Technical Library, Department 56)
3 Ordnance Research Laboratory, Pennsylvania State University, University Park
  Dr. B. W. McCormick (1)
  Dr. G. F. Wislicenus (1)
  Development Contract Administrator (1)
1 Pacific Aeronautical Library, Los Angeles
1 Philco Corporation, Philadelphia (Engineering Library) via RInsMat
1 Polytechnic Institute of Brooklyn (Department of Aeronautical Engineering and Applied Mechanics, Prof. A. Ferri)
1 Reed Research, Inc.
1 Rensselaer Polytechnic Institute, Troy, N. Y. (Department of Mathematics)
1 Republic Aviation Corporation, Farmingdale, N. Y.
1 Rose Polytechnic Institute, Terre Haute, Ind. (Dr. W. W. Clausen)

1 Scripps Institution of Oceanography, University of California, La Jolla
1 Society of Naval Architects and Marine Engineers, New York
2 Southwest Research Institute, San Antonio
  Director, Department of Applied Mechanics (1)
  Editor, Applied Mechanics Review (1)
2 Stanford University, Stanford, Calif.
  Department of Mathematics
    Head (1)
    Prof. B. Perry (1)
2 State University of Iowa, Iowa Institute of Hydraulic Research, Iowa City
  Prof. H. Rouse (1)
  Prof. L. Landweber (1)
1 Technical Research Group, New York (Dr. Paul Kaplan)
1 The Martin Company, Baltimore (Science Technical Library)
2 The Rand Corporation, Santa Monica, Calif.
  Dr. Blaine Parkin (1)
  Technical Library (1)
1 The University of Southern California, Los Angeles (Engineering Center, Dr. Raymond Chuan)
1 United Technology Corporation, Menlo Park, Calif. (Technical Library)
3 University of California, College of Engineering, Berkeley
  Prof. A. Schade (1)
  Prof. J. V. Wehausen (1)
  Prof. H. Einstein (1)
1 University of Illinois, Urbana (College of Engineering, Prof. J. Robertson)
1 University of Kansas, Lawrence (Dean, School of Architecture and Engineering)
1 University of Maryland, Institute of Fluid Dynamics and Applied Mathematics, College Park
3 University of Michigan, Ann Arbor
  Department of Civil Engineering, Prof. V. Streeter (1)
  Department of Engineering Mechanics, Prof. C. S. Yih (1)
  Department of Naval Architecture and Marine Engineering, Prof. R. B. Couch (1)
1 University of Minnesota, St. Anthony Falls Hydraulic Laboratory, Minneapolis
1 University of Notre Dame (Department of Engineering Mechanics, Prof. A. G. Strandhagen)
1 University of Wisconsin, Mathematics Research Center, Madison (Prof. L. M. Milne-Thomson)
1 Vitro Corporation of America, Silver Spring Laboratory, Silver Spring (Librarian)
1 Webb Institute of Naval Architecture, Glen Cove, N. Y. (Technical Library)

1 Westinghouse Electric Corporation, Baltimore (Engineering Librarian)
1 Westinghouse Electric Corporation, Sunnyvale, Calif. (M. Macovsky)
1 Westinghouse Research Laboratories, Pittsburgh
1 Woods Hole Oceanographic Institution, Woods Hole, Mass.

NOTS CL 629-61 280